Effects of Sway Motion on Smooth-Surface Vortex Separation Onset and Progression: Surface Combatant and Surface-Piercing Truncated Cylinder

Frederick Stern
IIHR-Hydroscience and Engineering University of Iowa
Iowa City, IA 52242
UNITED STATES OF AMERICA

frederick-stern@uiowa.edu

ABSTRACT

The effects of sway motion on smooth-surface vortex separation onset and progression is studied for both practical surface combatant 5415 and basic surface-piercing truncated cylinder geometries. Towing tank experiments include PMM force and moment measurements and for the surface combatant TPIV for the bow region and preliminary 4D-PTV. LES simulations for subcritical Reynolds and Froude numbers are conducted for the cylinder. The sway amplitudes and frequencies are based on previous 5415 and single-phase cylinder studies. TPIV results show the major vortices dynamic onset and progression with alternating strengths and signs in time and trajectories in space. At phases 0° and 90°, the results exhibit similarity with static drift β=0 (straight ahead) and 10°, respectively. At the intermediate phases, the measurements show transition between these two conditions and substantial vortex interactions and unsteady separation for dynamic maneuvering. Vortex core analysis using Q criteria of the sonar dome vortices shows sinusoidal oscillation with 1st-order harmonic amplitude decreasing with progression. The core trajectory is loop-shaped but exhibits rather complicated shape changes along the vortex progression. The cylinder results show similarities with single phase studies, but with substantial free surface effects. Drag and lift show increase with amplitude and frequency with phase jump at frequency ratio fr=1 due to switch from 2P to 2S vortex shedding. Fine grid LES shows reasonable agreement for force amplitudes, phases and FFT and phased averaged frequencies, which provides confidence in the flow field predictions, which are analyzed and compared with precursory straight-ahead experiments and LES; and single-phase controlled oscillation results. The 5415 results are being used by NATO AVT-253 for assessment of predictions methods and the cylinder results are being used for analysis of the physics of free surface boundary layer and wake/wave interactions and turbulence anisotropy; and for guidance for the analysis of the 5415 results. 4D-PTV for 5415 and additional analysis of the LES results for the cylinder are in progress.

1.0 INTRODUCTION

Smooth-surface vortex separation onset and progression is a ubiquitous flow feature and critical limiting factor for the design and operation of sea and air vehicles. Improvements in modeling and simulation capability are required to meet increased performance requirements and standardization of maritime regulations. For small amplitude static and dynamic maneuvers, both systems-based and physics-based CFD simulation method predictions are satisfactory; however, for large amplitude motions both approaches have difficulties, as shown by the results of the SIMMAN 2008 and 2014 Workshops (Stern et al., 2011; Simonsen et al., 2017).

Under the auspices of the AVT-183 Reliable Prediction of Separated Flow Onset and Progression for Air and Sea Vehicles significant progress was made for improved physical understanding and prediction capabilities for three-dimensional steady separation (NATO STO, 2017). The sea facet focused on large amplitude static drift β maneuvers for which benchmark validation experimental studies were conducted for surface combatant 5415

β=0, 10 and 20° (Yoon et al., 2014), KVLCC2 (very large crude carrier) β=30° (Abdel-Maksoud et al., 2015) and high-speed DC (Delft Catamaran) β=6°. (Broglia et al., 2019) and used as test cases for the assessment of the predictions. The verification and validation and uncertainty quantification (V&V and UQ) studies from 9 institutes used in-house and commercial codes resulting in 33 submissions. The submissions for 5415 (6 for β=0 and 8 for β=20°) involved fine grids with more than 45M points, thus the conclusions for this test case were the most reliable: RANS/URANS/DES indicated its ability to predict the onset but not progression of smooth surface vortex separation due to turbulence model deficiencies as RANS/URANS results were insensitive to grid refinement for grids greater than 50M cells (Bhushan et al., 2019). Vortex core location/axial velocity errors were relatively small, but vortex strength and TKE errors were very large. Large drift angle flow exhibits unsteady closed (leeward bow bubble separation with shear layer, Karman and breathing mode instabilities) and open (cross-flow separation vortices, which undergo helical mode instability and spiral vortex breakdown with similar scaling as delta wing tip vortices) separations. TKE budgets for the leeward bow bubble and sonar dome vortices have similarities with those for canonical flows and previous ship studies but show some differences in the role of transport terms. TPIV vortex core analysis was instrumental in reaching these conclusions.

Building on the AVT-183 progress, AVT-253 Assessment of Prediction Methods for Large Amplitude Dynamic Maneuvers for Naval Vehicles is extending the sea facet activities for dynamic maneuvers and improved physical understanding and prediction capabilities for three-dimensional unsteady separation. The focus is on benchmark validation experiments and prediction assessment for 5415 and JAPAN Bulk Carrier (JBC) in pure sway motion. The focus on sway vs. yaw motion was based on the benefit of building on previous static drift knowledge vs. larger importance of yaw vs. sway motion for maneuvering, as was focus in earlier studies (Yoon et al., 2015a, b). Herein the progress on the 5415 experiments is reported.

Fundamental studies using simplified geometries enable higher fidelity/resolution measurements and simulations of the physics of interest and useful for improvements in modeling and simulation capability for practical geometries. Fundamental studies relevant for surface ships include several simplified surface-piercing geometries with focus on various physics. Flat plate/foil model for boundary layer and wake/wave interactions, wave induced separation and low Froude number (Fr) free surface turbulence anisotropy (Stern et al., 1993; Longo et al., 1998). Truncated strut and cylinder models for wave induced separation (Xing et al., 2007), white-water wakes (Brandt et al., 2004) and subcritical and critical Reynolds number (Re) and Fr smooth surface bluff body and sharp edge bottom separation and low/high Fr free surface turbulence anisotropy (Stern, 2016). Wedge model for wave breaking air entrainment and spray (Wang et al., 2010). Transom stern model for sharp edge bluff body separation and free surface interaction (Drazen et al., 2010).

Herein, the surface piercing truncated cylinder straight ahead towing tank experimental and LES studies are extended for sway motion subcritical Re and Fr. The combination of both practical and simplified geometries is useful in assessing the state of the art for experiments and simulation capability smooth surface unsteady vortex separation.

2.0 SURFACE COMBATANT

The surface combatant experiments use the IIHR 3×3×100 m towing tank, PMM carriage/mount/load-cell, 3 m 5415 model (DDG51preliminary design) and previous TPIV and recent 4D-PTV measurement systems, as shown in Figures 2-1 and 2-2, respectively. The Fr=.28 and maximum sway amplitude is 10^o, which is the largest amplitude possible due to experimental limitations and corresponds to one of the steady drift angles previously investigated by Yoon et al. (2014). Test conditions meet the ITTC criteria for sway frequency and restricted water. The experiments were initiated (Yoon and Stern, 2017) using the same 3 m 5415 model condition and TPIV system as Yoon et al. (2014); however, the TPIV suffered an accident, which required its

replacement. Subsequently, the 3 m 5415 model was refurbished and the towed 4D-PTV system was designed, constructed and is currently under commissioning. Herein the results of Yoon and Stern (2017) are summarized and compared with the current results for surge, sway and yaw moment (X, Y, N) along with the status of the current progress in the commissioning of the 4D-PTV system.

2.1 5415 3 m model

The surface combatant 5415 geometry is an international benchmark for EFD validation data and CFD V&V, as described in Table 2-1 and shown in Figure 2-3 including the coordinate system for the measurements. The 3 m 5415 is also referred to as model 5512, which was constructed by NSWCCD as a geosym of their 6 m 5415 model. The original 5512 model was equipped with twin shafts/struts, propellers and rudders, although most of the benchmark data is for the bare hull initially without and subsequently with bilge keels. To initiate transition to turbulent flow, a row of cylindrical studs was attached at 0.05 L downstream of the forward perpendicular (FP) in accordance with the recommendations by the 23rd ITTC.

The 5512 model was 3D scanned using a FARO Arm laser scanner before any repairs were initiated. When comparing the 3D scan to an existing 3D model significant deviation was discovered (±2 mm over large parts of the hull, isolated areas up to ±5 mm). After removing the bilge keels an external framework was built around the model to allow the existing templates to be placed and removed while maintaining a precise location/alignment. Additional templates were created for the bow, stern, and sonar dome. Additional fiberglass and body filler was added where needed, and the model was shaped and sanded until all of the templates fit properly. The bilge keels, which were 3D printed in ABS plastic, where then bolted to the side of the hull using new templates to ensure accurate locations. The model was then 3D scanned and compared to the 3D model. Approximately 90% of the wetted surface is now within ±0.8 mm. Isolated areas are up to ±2 mm. Table 2-1 also provides the bilge keel offsets and Figure 2-4 shows the details of the bilge keel geometry and location and photo of the refurbished 5512 model.

2.2 Experimental Setup and Test Conditions

Two right-handed Cartesian coordinate systems are used. The xyz-coordinate system shown in Figure 2-3 (top) is a relative inertial frame of reference fixed to the moving model. The origin is at the intersection of the FP (forward perpendicular), hull centerline, and the calm-water plane. The $x_{\mathrm{PMM}}y_{\mathrm{PMM}}$ coordinate system shown in Figure 2-3 (bottom) is a non-inertial frame of reference fixed to the PMM carriage. The origin is at the intersection of the PMM centerline and the transverse axis of the PMM. The PMM centerline is the center of the oscillatory side-to-side sway motion. The x_{PMM} axis is parallel with the model towing direction and positive to upstream. The y_{PMM} axis is normal to the x_{PMM} axis and positive to starboard. The xyz-coordinate system is used for the TPIV measurements along the hull and the $x_{\mathrm{PMM}}y_{\mathrm{PMM}}$-coordinate system is used to describe the pure sway motion. Yoon et al. (2015a) provide the relationship between these two coordinate systems.

The PMM is a Scotch-yoke type mechanical system and converts rotational motion of an 11 kW AC servo motor to linear sway and rotary yaw motions. Initially, the Scotch-yoke has been driven up to 0.25 Hz with maximum sway and yaw amplitudes of 500 mm and 30°. Recently, an upgrade was made to allow frequencies higher than 1 Hz by adding a gearbox of 1:3 ratio, for an oscillating surface-piercing truncated cylinder experiment to extend its precedent test case of steady towing (Stern, 2016). Linear and rotary potentiometers monitor and report the sway and yaw positions.

The PMM motions are described by the sway amplitude y_{max}, yaw amplitude ψ_{max}, PMM frequency f, and drift angle β as

$$y_{PMM} = -y_{max} \sin(2\pi f t) \quad (1)$$

$$\psi = -\psi_{max} \cos(2\pi f t) + \beta \quad (2)$$

in combination with $x_{PMM} = U_C t$, where U_C is the towing speed and t is time. The heading angle ψ is the angle between the model centerline and the model towing direction.

Table 2-2 provides a summary of test conditions. The tests are conducted at one towing speed U_C = 1.531 m/s corresponding to a Fr = 0.28. The Re = 4.65 × 10^6 is based on a nominal water temperature of 20 °C for Yoon and Stern (2017) and Re = 4.458 × 10^6 to 4.514 × 10^6 are based on a nominal water temperature of 18.2 to 18.7 °C for the current experiments. The yearly water temperature variation in the IIHR towing tank is approximately between 8 and 23 °C. For Yoon and Stern (2017) the model is restrained from all free motions[1], i.e., fixed to a sinkage σ = 1.92 × 10^{-3} L and trim τ = -0.136° (positive bow up) corresponding to the dynamic sinkage and trim in steady straight-ahead towing at the same Fr, whereas for the current experiments σ = 0.0 L and trim τ = 0°. Pure sway motions of three different maximum sway velocity v_{max} = 0.034, 0.070, and 0.176 U_C cases are tested for forces and moment measurements. These v_{max} values correspond to maximum drift angle β_{max} = $\tan^{-1}(v_{max}/U_C)$ = 2, 4, and 10°, respectively. Whereas, the TPIV measurements are conducted for only one v_{max} = 0.176 (i.e., the β_{max} = 10°).

The PMM sway amplitude y_{max} and frequency f are adjusted in combination accordingly to the relationship $v_{max} = y_{max}\omega$, where $\omega = 2\pi f$. Table 2-3 shows the y_{max} and f combinations used for the experiments. For forces and moment measurements, three sway amplitudes y_{max} = 0.021, 0.042, and 0.104 L values are used with the frequency fixed at f = 0.134 Hz, corresponding to β_{max} = 2, 4, and 10°, respectively. These conditions were originally selected by three organizations FORCE/DMI, CNR/INSEAN, and IIHR in collaboration for the 24th-25th ITTC Maneuvering Committee and the SIMMAN 2008 and used herein for the present forces and moment measurements for direct comparison of the results. For the TPIV measurement, the sway amplitude is limited to a smaller y_{max} = 0.087 L avoiding interference of the TPIV assembly with the tank wall while measuring the far field flow. Accordingly, a faster frequency f = 0.162 Hz is used to keep the β_{max} = 10° condition.

Yoon and Stern (2017) provide detailed (1) discussion/evidence that the test conditions meet the ITTC criteria for sway frequency and restricted water; (2) measurement systems; (3) TPIV synchronization; (4) data acquisition; and (5) uncertainty assessment for forces and moment and TPIV. (1) is the same for the current tests as is the load cell; however, the PMM carriage/load cell and 4D-PTV and its synchronization and data acquisition procedures are different, as discussed in Section 1.2.5. Uncertainty assessment for the current experiments is in progress.

2.3 Forces and Moment

2.3.1 Yoon and Stern (2017)

Forces and moment measurement use a 6-component strain-gage type loadcell and a 6-channel signal amplifier. The measurement ranges are 500 N commonly for all three force components, 50 N-m for pitch and roll moments and 200 N-m for yaw moment. The loadcell is calibrated statically on a test stand using standard weights.

[1]This condition is the $FX_{\sigma\tau}$ mounting condition of Yoon et al. (2015a).

The forces and moment data show differences of 2-6 %D compared to the previously published data, which are usually within their uncertainty limits of 2-8 %D. Thus, the two data sets are considered as consistent with one another. However, their FS coefficients show discrepancies about 3% that is larger than their UA limits of about 1%. The UA shows the most critical source of the error is the uncertainty associated with the sway frequency setting. Care is needed for the frequency setting with a higher accuracy.

2.3.2 Current Results

For carriage driving, inverter-controlled AC motor is used at IIHR towing tank. In the previous experiments, the carriage speed was controlled by changing input voltage to built-in AD converter of the inverter. The input voltage was changed by a potentiometer on the carriage operator with 100 meters length cable from the potentiometer to the inverter. The inverter can control motor output that is proportional to the input voltage signal. The input voltage signal affected by the aging of the cable and environmental noise and this may cause voltage and velocity fluctuations. To improve this situation, we use a digital operator to control the inverter in the present experiments. With the digital operator, we can input desired motor output ratio in percent to full output numerically and send start and stop commands to the inverter. The inverter feed-back control keeps setting motor output by the digital operator. However, there is no feedback control for actual carriage speed. Therefore, calibration between input motor output value and the actual carriage speed is performed by a photosensor and reflectors. The reflectors are located at 6 points along the tank and the photosensor equipped on the carriage can detect the locations. We also recalibrated the carriage velocimeter and updated velocity uncertainties, but the results will be presented in the future. To keep reliable wired communication between the inverter and digital operator, the communication cable is also improved to reduce the noise. With this new control method and new calibration, we can guarantee carriage speed with 3 decimal points.

During the PMM operation, the servo motor is one of the main noise sources which affects signal from the loadcell. To reduce the noise, the loadcell is isolated from the PMM carriage and all the cables connected to the servo motor are covered by aluminum shield film for EMI noise reduction. Noise level has been improved with these treatments, but we can still observe a voltage shift during the PMM operation for surge X and sway Y forces. To evaluate this voltage shift, shunt calibrations were performed with the PMM lever set to zero (i.e. sway motion is zero and motor is idling.) before and after the experiments with the carriage stopped. In this paper, the averaged X values during PMM operation without advance speed are treated as actual zero point of X.

The digital operator has been modified so that the carriage can automatically start and stop by an external trigger signal from a microcontroller. This modification enables management of the carriage running time and stop location. Two microcontrollers are used for force measurements under the pure sway condition. The microcontroller 1 with extended 16 bits AD converter keeps monitoring voltage signal from the sway potentiometer on PMM carriage. The microcontroller 2 controls the carriage start and stop operations based on the signal from the microcontroller 1. In the actual experiments, the carriage was started when sway reached to the specific phase and the carriage was stopped after desired duration. These controllers are also used for 4DPTV experiments.

Figure 2-5 and Table 2-4 provide straight ahead X results for Fr = 0.140, 0.281 and 0.409. Maximum error between previous and present X is within 4%. Table 2-5 and Figure 2-6 show static drift surge and sway forces roll and yaw moments. The maximum asymmetry error between positive and negative β for X, Y, K and N are 2%,0.5%,6% and 10%, respectively, as shown in Table 2-6. Table 2-7 and Figure 2-7 show FS sine and cosine coefficients of pure sway X, Y and N for all conditions. In Figure 2-7, data taken under SPIV and TPIV conditions are shown as in green and blue, respectively, and the previous and present regression curves are shown in black and orange, respectively. Figure 2-8 shows reconstructed time series comparisons for X, Y, N at

β_{max} = 10°. Table 2-8 and 2-9 show comparison between present and two previous data sets at β_{max} = 10°. The errors between the previous and present data are about 20 to 30% for X_0 and about 200% for X_{C2}. As for X_0, the previous data is within present random error bars. Due to larger X_{C2}, X amplitude of reconstructed time series is larger than previous as shown in Figure 2-8. For Y_{C1}, N_{C1}, Y_{S1} and N_{S1}, the error between present and the previous data taken in 2017 is smaller than that in 2015. The reconstructed results of Y and N in Figure 2-8 are all within the previous uncertainty range. The reason why X_{C2} becomes larger than the previous data is still under investigation. Asymmetry bias analysis for pure sway condition is still under processing and will be presented in final paper.

2.4 TPIV Results

The TPIV is a towed underwater Tomographic PIV (TPIV) system by LaVision. The TPIV consists of four Imager pro SX 5M-pixel CCD cameras, a dual-head Nd:YAG laser, a sub-merged light-sheet generator, and DaVis8 software. The highest frame rate of the cameras is 14.2 frames per second (fps) when the highest pixel resolution is used. For the present study, a 2×2 hardware pixel-binning is used to achieve a faster camera frame rate of 26 fps. Each camera is equipped with a Nikkor 50 mm f/1.8D lens along with motors for remote focusing and aperture adjustments. The cameras are also equipped with motors for remote Scheimpflug angle adjustments. The laser is a CFR400 model by Quantel with a 190 mJ/pulse power and the maximum pulse repetition rate of 15 Hz. The TPIV system enables volumetric flow measurements and the acquisitions of all the 3-dimensional components of the velocity, turbulence, and vorticity variables. The volume data also allows vortex core analysis using the Q-criteria and in-depth analysis of vortex separation onset and progression in combination with the CFD.

For phase-averaged TPIV, conventional uncertainty estimation methods can be difficult to implement. Instead, the present UA used practical methods by using uniform inflow calibration results for systematic uncertainty and statistical convergence errors for random uncertainty. The results show the uncertainties are about 1-3 %U_C for the velocity variables and about 16% for the turbulence variables, which are comparable with the earlier UA results published.

CFD results are used to identify the vortices. The major vortices include sonar dome vortex (SDV) and sonar dome tip vortex (SDTV) shedding from the sonar dome bow, fore-body keel vortex (FBKV) separating along the fore-body keel, bilge keel vortex (BKV) and bilge keel tip vortex (BKTV) shedding from the port and starboard bilge keels, and aft-body keel vortex (ABKV) separating along the hull aft-body.

Steady flow TPIV results show reasonable comparisons with the previous measurements using the same model and the same TPIV system. A more advanced TPIV algorithm (the fast-MART) used for the present TPIV allowed the present TPIV for improved measurements close to the hull surface and less spurious data compared to the previous results.

The pure sway TPIV results show the major vortices dynamic onset and separation with alternating their strength and sign in time and translation in space. At phases 0° and 90°, the measurement results exhibit close similarity with the steady flow measurements but at the same time dissimilarity as well. At the intermediate phases, the measurements show transitional flow and substantial vortex interactions and unsteady separation onset and progression for dynamic maneuver.

Vortex core is defined by using the Q criteria, which is possible for the TPIV with volume data. The core ω_x of SDTV is sinusoidal oscillation of which 1st-order harmonic amplitude decreasing with the vortex progression to downstream. The core trajectory is typically loop-shaped but exhibits rather complicated shape changes along

the vortex progression. The core variables exhibit close similarities with those of the static drift 10° results but dissimilarities with the pure yaw 10° heading results, in terms of the maximum ω_x and the locations of the core. The Appendix A-1 provides recent reanalysis of the SDTV core trajectory reconstructions that were done for and have been provided to AVT-253.

The current progress on the present experiment is limited to only two x-stations. However, the results are reliable as detailed in this paper and already used to guide the CFD simulations for AVT-253.

2.5 4D-PTV Results

The 4DPTV is a towed underwater 4-dimensional Particle Tracking Velocimetry (4DPTV) system by LaVision. The 4DPTV consists of four MiniShaker 2M-pixel CCD cameras, Nd:YLF Single Cavity Diode Pumped Solid State, High Repetition Rate Laser with chiller, a sub-merged light-sheet generator, and DaVis10 software. The highest frame rate of the cameras is 121 frames per second (fps) when the highest pixel resolution is used. For the present study, 800 × 600-pixel resolution is used to achieve a faster camera frame rate of 600 fps. Each camera is equipped with pre-calibrated lens and mirror and there is no need for Scheimpflug angle adjustments as SPIV and TPIV. The laser is a DM30-527 model by Photonics Industries International, Inc with a 30 mJ/pulse power and the maximum pulse repetition rate of 10 kHz. The measurement volume size is 210 mm length × 150 mm width and 240 mm height, respectively. The total number of vectors within the measurement volume is 58 × 41× 66 with a spatial resolution of about 3.7 mm between the adjacent vectors in all directions.

Before starting measurement flow field around 5415 by 4DPTV, uniform flow measurements are performed with various conditions to evaluate measurement accuracy of 4DPTV by comparing with results obtained by the carriage velocimeter. To control particle densities and seeding locations, the photo sensor and reflectors are used as start trigger of 4DPTV system for uniform flow measurements. For pure sway condition, the newly developed trigger system described in 2.3.2 is also used for 4DPTV measurements to control initial phase of sway motion.

The measured velocities by 4DPTV shown as following Tables and Figures are mean value of valid vectors in the entire measurement volume. Table 2-10 and Figure 2-9 show summary of uniform flow measurements for 6 different carriage speed. Averaged error between speed over ground by carriage velocimeter and uniform flow velocity magnitude |U| by 4DPTV is 0.57% and the averaged angle between sway velocity (u) and the sway velocity (v), $Tan^{-1}(v/u)$ is 1.28°. Table 2-11 shows summary of static drift uniform flow results when the carriage speed is 1.535 m/s. The averaged difference between U_C and |U| by 4DPTV is 0.43% as small value as in uniform flow measurements. Figure 2-10 shows relationship between setting drift angle β and $Tan^{-1}(v/u)$. Averaged difference between setting β and $Tan^{-1}(v/u)$ is 0.97°. Table 2-12 provides uniform flow measurement results under the same pure sway condition as TPIV in previous study. Figure 2-11 shows timeseries comparison between PMM sway velocity and sway velocity component (v) obtained by 4DPTV. In Table 2-12, U_0, u_0, v_0, w_0 and v_1 are 0^{th} and 1^{st} harmonic amplitudes of velocity components obtained by Fourier analysis which fundamental frequency is pure sway frequency 0.162. Figure 2-12 shows 0^{th} to 6^{th} harmonic v amplitudes. Averaged angle $Tan^{-1}(v_0/u_0)$ is -1.18° and the averaged difference between v_1 and 1^{st} harmonic sway motion velocity (V_{sway1}) is 7.7%.

As shown in Figure 2-11, phase difference is observed between PMM sway velocity and v measured by 4DPTV even the same start trigger was used. This is caused by 4DPTV system delay. In the actual 5415 experiments, we will use new synchronized DAQ recording system and this delay will be improved in the future experiments.

The camera calibration and PMM strongback alignment are the possible error factors that give Tan-1 (v / u)

around 1 ° and the further investigation is needed.

Uniform flow measurements without ship model are performed to evaluate accuracy of new 4DPTV system. It has been confirmed that new 4DPTV system can perform measurement with high accuracy as conventional SPIV and TPIV in uniform flow measurements. Statistical convergence error analysis of TKE is still under going to determine minimum requirement of frame numbers to get converged results. We will start flow field measurements around 5415 in July and complete results using the 4D-PTV will be included in the final paper. Preliminary URANS/DES assessment indicates difficulties in predicting the vortex interactions.

3.0 SURFACE-PIERCING TRUNCATED CYLINDER

The component problem of cylinder flow has relevance in ship hydrodynamics/marine engineering, ocean engineering, building aerodynamics and hydraulics. The present focus is on surface ship boundary layer and wake/wave interactions for surface-piercing 3D smooth surface bluff-body separation: (1) air-water interface effects on vortex shedding and turbulence anisotropy; (2) wave breaking, air-entrainment and spray; and (3) sharp-edge bottom effects. The approach integrates high-fidelity towing tank experiments and LES for measurement-system/code development and assessment physics and high-fidelity experimental and simulation capabilities. The goal is to achieve practical geometry model scale experiments and LES for detailed resolution of turbulence, vortex structures and bubble/droplets/spray for physical understanding and guide development RANS models.

The LES of Suh et al. (2011) and Koo et al. (2014) explained previously observed free surface effects of wake spreading and attenuation of Karman vortices, as the result of longitudinal vortices induced by turbulence anisotropy; however, experimental data was lacking for validation. Although the direct measurement of the turbulence anisotropy is not yet achieved for a surface-piercing cylinder, Stern (2016) provides additional and arguable strong evidence via integrated towing tank measurements and LES for a truncated cylinder (aspect ratio 4) for subcritical and critical Re and Fr. The measurements include unsteady loads, mean surface pressure and mean and RMS wave elevations and SPIV. The LES includes multi-block, fine/medium grids and V&V for subcritical/critical Re and Fr. The grids were based on single-phase LES studies for subcritical to supercritical Re, including prediction of the drag crisis (Yeon et al., 2016), however, it was not possible to also implement conservative convection schemes due to its instability across the interface. The focus is on the boundary layer and wake/wave interactions including natural transition, closed/open separation instabilities and air-water interface turbulence anisotropy. The overall results confirm and expand on previous findings in clarifying the difference in the air-water interface anisotropy for low and high Fr, i.e., due to damping and augmentation of the normal fluctuations, respectively, under the assumption that the LES is sufficiently validated for the measured variables to provide confidence in the simulations in toto. Yoon et al. (2019a) updates Stern (2016) for additional SPIV (for z = -3.5), LES (medium grid for critical Re/Fr), FFT (for combination bottom and Karman frequencies) and critical Re/Fr surface pressure analysis.

Herein, the experiments and LES are extended for sway motion. Sway motion is important for surface ships as already discussed and dominant component for VIV and undergone extensive studies for single phase flows both for controlled and free oscillations. Studies for surface-piercing bodies are limited.

3.1 Experimental Methods

The cylinder experiments (Figure 3-1) use the same towing tank, PMM carriage/mount/load-cell and setup as described previously for the surface combatant experiments with the same cylinder model as Stern (2016). The model is made of Plexiglass with diameter D=.2 m and AR=L/D=4. The cylinder drag C_D and lift C_L were measured for sway amplitudes A/D=0.5 and .25 and range of frequencies f_e below, equal and larger than the

Karman frequency, i.e., frequency ratio $0.75 \leq fr=f_e/f_K \leq 1.25$. f_K is the measured $St=f_KD/U$ for the straight-ahead condition for corresponding Re/Fr. The carriage speed was adjusted due to temperature differences to have the same Re as Stern (2016), i.e., for subcritical Re=123k and for critical Re=270k and an additional Re=27k was done for comparisons with single-phase sway experiments. Straight-ahead test was conducted to confirm the current setup via. comparisons with previous data. Since the temperature was similar as for the previous test the Fr were nearly the same and the C_D, C_L and St values were within the RSS of both experiments SD. For critical Re the fe values are very large up to 1.2 Hz, which would have required strengthening of the PMM carriage and thus deferred. Table 3-1 provides the test matrix. The Re adjusted Fr = .093 and .423 vs. .1 and .5, respectively, as used for the current LES. Thus, these Fr differences need to be considered in the present LES validation. The maximum sway velocity and angle of attack are very large ranging from 40 – 60%U and 22 – 34° for the lowest to highest fr. Test conditions meet the ITTC criteria for restricted water, but not sway frequency except for lowest Re and Fr since for larger Re and Fr f_e is larger than usual quasi-steady values used for ship maneuvering PMM testing. Figure 3-2 overlays the current experimental conditions on the single-phase controlled oscillations map of the vortex wake modes. Note that $\lambda/D = Ste^{-1} = U/feD$. The map suggests for the larger fr 2S (Karman) and for the smaller fr 2P vortex shedding. For Karman two alternate rotating vortices are shed (one from each side of the cylinder) for each period, whereas for 2P two alternate vortices are shed from each side for each period, i.e., 2S sheds 2 and 2P sheds 4 vortices per period.

The validation variables are the drag C_D and lift C_L forces for specified A/D and fe. The sway motion *y*, C_D and C_L equations are:

$$y(t) = Asin(2\pi f_e t) \tag{3}$$

$$C_D(t) \approx C_{D1} sin[2(2\pi f_e t + \phi_D)] + C_{D0} \tag{4}$$

$$C_L(t) \approx C_{L1} sin(2\pi f_e t + \phi_L) \tag{5}$$

Mean C_D and C_D and C_L first harmonic amplitudes and phases were evaluated and compared with single-phase data. FFT and phase averaging was also done to identify the dominant frequencies. Video was taken for observations of the wave patterns.

3.2 LES Methods

An orthogonal curvilinear non-uniform staggered grid solver, CFDShip-Iowa Version 6.2 is used for the simulations. The code was extended from the sharp interface two-phase Cartesian grid solver Version 6.1 (Yang and Stern, 2009) in which the level set method is used for the air/water interface tracking and an immersed boundary method (IBM) is used to handle complex geometries on Cartesian grids. Lagrangian dynamic subgrid-scale (SGS) model is adopted for large-eddy simulation (LES). A finite difference method is used to discretize the Navier–Stokes equations and time advancement is based on the semi-implicit four-step fractional step method. The convective terms are discretized using the third-order QUICK and fifth-order WENO schemes with semi-Lagrangian advection schemes also implemented. All other terms are discretized with the standard second-order central difference scheme. The pressure Poisson equation is solved using the HYPRE library (Falgout et al., 2006). The code parallelization is done via a domain decomposition technique using the MPI library. Parallel I/O using MPI2 has been implemented (Yang et al., 2008). A coupled level set and VOF (CLSVOF) method was implemented (Wang et al., 2009) for the interface tracking to improve the mass conservation property. Suh et al. (2011) extended the code from Cartesian grid to orthogonal curvilinear grid where the level set method was still used for the interface tracking and the IBM method was eliminated. The CLSVOF method was implemented by Wang et al. (2012a) to the orthogonal curvilinear grid with applications to an interface-piercing circular cylinder

(Koo et al., 2014), which was soon replaced by the new VOF methods (Wang et al., 2012b, c). Recently, capabilities of multi-block (Yoon et al., 2016) have been implemented and applied to simulations of a surface-piercing truncated cylinder (Stern, 2016). The static overset grids have also been implemented and used for the current simulations as described by Yoon et al. (2019b), including discussion of the accuracy of overset vs. non-overset grids.

Figure 3-3 shows the computational domain, boundary conditions and overset grids used for the simulations and Table 3-2 summarizes the CFD test cases and status. Overset grid system comprises two parts: background and cylinder grids. A rectangular domain is used for the background grid. The *x*-, *y*-, *z*-coordinates are consistent with the experiment, directing to downstream, transversely to starboard, and upward, respectively. The coordinate system is non-dimensionalized using the cylinder diameter. Herein, a non-inertial reference frame is used to handle the oscillating cylinder motion with the static overset grid algorithm. Thus, the coordinate system is fixed at the cylinder and the whole domain moves with the cylinder. The source term for the non-inertial reference frame is implemented as follows

$$\frac{\partial \mathbf{u}_r}{\partial t} + \mathbf{u}_r \cdot \nabla \mathbf{u}_r = -\frac{1}{\rho}\nabla \cdot (p\mathbf{I} + \mathbf{T}) + \mathbf{g} - \mathbf{f} \tag{6}$$

$$\mathbf{f} = \frac{d^2\mathbf{x}_g}{dt^2} + \frac{d\boldsymbol{\Omega}}{dt} \times \mathbf{x}_r + 2\boldsymbol{\Omega} \times \mathbf{u}_r + \boldsymbol{\Omega} \times (\boldsymbol{\Omega} \times \mathbf{x}_r) \tag{7}$$

where $\mathbf{x}_r$ and $\mathbf{u}_r$ are position vector and velocity vector in noninertial reference frame, respectively, $\mathbf{x}_g$ is a displacement vector between inertial reference frame and noninertial reference frame. $\boldsymbol{\Omega}$ is the angular velocity vector of the non-inertial reference frame with respect to a stationary inertial reference frame. For the present simulation, $\boldsymbol{\Omega}$ = 0 and the acceleration term for the transverse motion is added to the momentum equation. The domain size for background grid is (streamwise, transverse, vertical) = (40D, 40D, 10D). For the grid near the cylinder (cylinder grid), a cylindrical coordinate system is used with the center of the cylinder at r=0 and the outer boundary at r=5D. The cylinder grid is overlapped on top of the background grid. The inflow/outflow boundary conditions are applied at the left/right side of the background grid. Slip wall boundary condition is applied at the rest of the boundaries (top/bottom and sides) for the background grid. The cylinder surface is considered as a no slip wall. Slip wall boundary condition is imposed at the top of the cylinder grid. The outer boundary at r=5D and the bottom for the cylinder grid are internal boundaries for the overset grid system. While coarse grids (0.5M, 0.7M) are used for Re=27k, coarse (1.6M) / medium (6.8M) / fine (13M) grids are used for Re=123k to verify the simulations and to study further details with fine resolution. The grids are systematically refined with non-uniform scale factors. The near wall grid spacing is r+=1.6 and 0.7 for the medium and fine grid, respectively, which is designed to be comparable to r+=1.4 and 0.88 for the previous subcritical LES with the multi-block medium and fine grid (Stern, 2016).

3.3 Verification and LES Quality

The overall verification & validation approach follows Stern et al. (2001) with updated factor of safety verification method (Xing and Stern, 2010). Solutions on three grids are completed for 10 vortex-shedding cycles and verification analysis is shown in Table 3-3. $U_I/|\varepsilon_{21}|$ is small. U_G is mostly small < $10\%S_1$, except for a few variables. The quality of the LES is assessed by evaluating the turbulent energy spectra at points in the shear layer and in the vortex formation region as shown in Figure 3-4. The fine grid Kolmogorov -5/3 scaling is achieved up to the grid cut-off.

3.4 Global Variables

Figure 3-5 compares the experimental C_D and C_L with benchmark single-phase data and the LES. The experiments show similar trends with single phase, but smaller amplitudes for C_D and C_L (for larger fe/f_K), e.g., 50% smaller C_{D1} and 22% smaller C_{D0} (cf. 30% smaller mean C_D for straight ahead), which is attributed to finite AR/bottom and free surface effects. C_{D1}, C_{L1} amplitudes increase for increasing fr and A/D (especially for high fr), whereas A/D effects are not significant for phases. The phases show similar out of phase and in phase response with jump at fr=1, as single-phase results associated with 2P vs. 2S vortex shedding for low vs. high fr. The effects of Re are small, as expected for subcritical range. The SD is large for C_D (42%D) and small for C_L (5%D).

The LES follows the trends of the experiments with reasonable errors considering the current grid sizes, i.e., for the phases and C_{D0} for all fr and for C_{D1} and C_{L1} for the highest fr the errors are reasonably small, whereas for C_{D1} and C_{L1} for the lower fr the errors are larger, as shown in Table 3-4.

C_D and C_L dominant frequencies were evaluated using FFT and triple decomposition

$$f(x,\ t) = \bar{f}(x) + \tilde{f}(x,t) + f'(x,t) \tag{8}$$

$$\langle f(x,t)\rangle = \lim_{N\to\infty}\frac{1}{N}\sum_{n=0}^{N-1} f(x,t+n\tau) \tag{9}$$

$$\langle f(x,t)\rangle = \bar{f}(x) + \tilde{f}(x,t) \tag{10}$$

$$\bar{f}(x) = \lim_{N\to\infty}\frac{1}{N}\sum_{n=0}^{N-1} f(x,t_0+n\Delta t) \tag{11}$$

The FFT analysis for Re=27k and 123k showed 2fe and subharmonics of 2fe for C_D, whereas for C_L only fe was dominant. The triple decomposition for Re=27k showed 2fe and subharmonics for C_D and fe and both sub and super harmonics of fe for C_L. The results for Re=123k were similar for C_D but for C_L no sub or super harmonics of fe are evident. The LES FFT and triple decomposition analysis shows similar dominant frequencies. For straight-ahead the FFT analysis indicated not only f_K but also a low frequency due to bottom separation f_b and combination frequencies $\Delta f = \pm nf_k \pm mf_b$, which were expected but not yet identified for the sway condition.

3.5 Photo, Mean and RMS Air/Water Interface

Figure 3-6 shows a rear-view photo of the experiment and LES visualization at the y_{max} position of the cylinder motion for A/D=0.5, fr=1.25 and phase $\varphi=\pi/2$ (t=T/4). The bow wave and ruffled wake are substantially more disturbed and unsteady compared to the straight-ahead condition for all fr; and with wave breaking for the highest fr. The LES is qualitatively similar but lacks resolution of the wave breaking.

The mean and RMS wave elevations are similar and substantially different than the straight-ahead condition for low vs. high fr, as highlighted in Figure 3-7, which shows the perturbation mean and RMS wave elevations, i.e. with straight ahead condition values subtracted. For low fr the mean wake trough depth and Kelvin waves are increased, whereas for high fr a large swept back bow wave and increased wake trough depth are predominant.

The RMS wave elevations are large in regions where the mean perturbation wave elevations are large. The phase averaged wave elevations show in phase anti-symmetric crests and troughs on the windward vs. leeward sides.

3.6 Surface Shear Stress, Pressure and Streamlines

Figure 3-8 shows side views of the surface shear stress with separation angle θ_S and regions of free surface, quasi-2D and bottom effects labeled; and surface pressure contours with overlaid streamlines. Table 3-5 summarizes the separation angles and regions. In the free surface effects region, the separation angle moves forward at the free surface (θ_S=74° for straight ahead, θ_S=67°, 51° and 18° for fr=0.75, 1.00, and 1.25, respectively) and is delayed below with increasing amounts for increasing fr. In the quasi-2D region, θ_S is constant with delayed values than for straight ahead. In the bottom region, θ_S is delayed. For low fr, the pressure is lowest near the bottom similarly as for straight-ahead, whereas for high fr the pressure is lowest near the free surface.

Figure 3-9 shows the circumferential distributions of Cp, including the previous straight-ahead subcritical experiments and LES for comparisons. The current straight-ahead Cp is lower, especially near θ=90°, which is attributed to the relatively coarse grid resolution and overset interpolation error; and the current Cp for sway shows lower base pressure. For straight ahead and low fr the base pressure near the free surface is higher than that near the bottom, whereas for high fr the base pressure near the free surface is lower than that near bottom.

3.7 Vortex Structure and Turbulence

Figure 3-10 shows mean Q=0.04 vortex structures side and top down views with mean vertical velocity W contours. The separation region x<2D has reduced large scale structures, whereas the wake region x>2D has increased smaller scale structures for increasing fr. Strong upwash behind the cylinder is observed in the bottom region for the straight ahead condition, whereas the upwash/separation region behind the cylinder become weaker/smaller, but tip vortices are stronger in the bottom region for sway motion. The shear layer angle on the free surface increases as fr increases: α_{fs}=60° for straight ahead, α_{fs}=74°, 79° and 87° for fr=0.75, 1.00, and 1.25, respectively, as shown Table 3-6. The bottom vortices angle increases as fr increases: α_b=24° for straight ahead, α_b=34°, 38° and 44° for fr=0.75, 1.00, and 1.25, respectively, as shown Table 3-7. Phase averaged Q=2 vortical structures (not shown) highlight the 2P 180° out of phase vs. 2S in phase vortex shedding.

Figure 3-11 shows the mean streamwise velocity on the center plane with overlaid streamlines. Consistent with the Q vortex structures, the mean separation region behind the cylinder substantially reduces for increasing fr. The extent of the bottom closed separation bubble height is 15%D explains the single-phase observations that for gap ratio g/D > 0.15, free end effects, i.e., increased fluid excitation force occurs, whereas for smaller values end plate effects are small. Streamwise and vertical RMS velocities are large in the separation region. The contours of mean streamwise velocity and TKE in horizontal planes show that the TKE in the wake region increases significantly for higher fr. Separation bubble size and high TKE region at z=-3.5 are smaller than those near the free surface.

Figure 3-12 shows the phase averaged vorticity for the three vertical locations z=-0.75, -2.00, -3.50 when the cylinder is at y=ymax. Near the free surface z=-0.75, wake modes are not distinctly shown due to wake spreading and attenuation. In the quasi-2D region z=-2.00, transition between two different wake modes (the low- and high-frequency modes) is clearly observed as fr increases, which is consistent to previous single-phase flow studies. The low-frequency wake mode generates long attached shear layers and makes a counter-rotating pair (2P mode of vortex shedding). The high-frequency wake mode has a much shorter wake length and vortices are shed in the 2S or Karman mode. In the bottom region, the wake becomes remarkably short due to upwash

and does not show any clear vortex shedding.

Figure 3-13 shows streamwise and transverse vorticity, normal Reynolds stress and turbulence anisotropy (term *E* defined in Stern (2016) for the Reynolds averaged vorticity transport equation analysis due to 2nd order cross derivative differences in the normal Reynolds stresses) at x=1. Mean streamwise velocity (not shown) highlights the closed separation regions for both straight ahead and sway, but the reverse flow in the separated region is smaller for sway in the quasi-2D and the bottom regions. Mean transverse velocity (not shown) shows outward flow near the free surface. Mean vertical velocity shows strong upwash near the bottom along y=0 (up to 45% of the streamwise velocity) and downwash in the mid span around -0.5<y<-1.0 (up to 20% of the streamwise velocity). The mean vertical velocity (not shown) near the free surface remains relatively stationary (less than 5% of the streamwise velocity). Streamwise vorticity ω_x shows the turbulence anisotropy induced counter clockwise vortex near the free surface and transverse vorticity ω_y is large counter clockwise near the free surface and bottom. Compared to straight ahead, the maximum values of $\overline{uu}$ and $\overline{uv}$ increase more than 4 times. $\overline{vv}$ near the free surface increases noticeably as fr increases. $\overline{ww}$ near the free surface increases slightly as fr increases. As a result, $\frac{\partial^2}{\partial y \partial z}(\overline{vv} - \overline{ww})$, the main production mechanism of the mean streamwise vorticity, significantly increases near the air/water interface as fr increases.

4.0 OVERALL CONCLUSIONS AND FUTURE RESEARCH

The effects of sway motion on smooth-surface vortex separation onset and progression is studied for both practical surface combatant 5415 and basic surface-piercing truncated cylinder geometries. Towing tank experiments include PMM force and moment measurements and for the surface combatant TPIV for the bow region and preliminary 4D-PTV. LES simulations for subcritical Reynolds and Froude numbers are conducted for the cylinder. The sway amplitudes and frequencies are based on previous 5415 and single-phase cylinder studies. TPIV results show the major vortices dynamic onset and progression with alternating strengths and signs in time and trajectories in space. At phases 0° and 90°, the results exhibit similarity with static drift β = 0 (straight ahead) and 10°, respectively. At the intermediate phases, the measurements show transition between these two conditions and substantial vortex interactions and unsteady separation for dynamic maneuvering. Vortex core analysis using Q criteria of the sonar dome vortices shows sinusoidal oscillation with 1st-order harmonic amplitude decreasing with progression. The core trajectory is loop-shaped but exhibits rather complicated shape changes along the vortex progression. The cylinder results show similarities with single phase studies, but with substantial free surface effects. Drag and lift show increase with amplitude and frequency with phase jump at frequency ratio fr=1 due to switch from 2P to 2S vortex shedding. Fine grid LES shows reasonable agreement for force amplitudes, phases and FFT and phased averaged frequencies, which provides confidence in the flow field predictions, which are analyzed and compared with precursory straight-ahead experiments and LES; and single-phase controlled oscillation results. The 5415 results are being used by NATO AVT-253 for assessment of predictions methods and the cylinder results are being used for analysis of the physics of free surface boundary layer and wake/wave interactions and turbulence anisotropy; and for guidance for the analysis of the 5415 results. 4D-PTV for 5415 and additional analysis of the LES results for the cylinder are in progress.

ACKNOWLEDGEMENT

Office of Naval Research grants N00014-17-1-2083 and N00014-17-1-2084 under administration Drs. Thomas Fu, Woei-Min Lin and Ki-Han Kim sponsored this research. The simulations were performed using DoD, Navy DSRC HPCMP resources including 18 Pathfinder program allocations. Drs Yugo Sanada, Sung-Hwan Yoon, Hyunse Yoon, Shota Yoneda and Zhaoyuan Wang are non-NATO country citizen co-authors.

REFERENCES

Abdel-Maksoud, M. , Müller, V. , Xing, T. , Toxopeus, S. , Stern, F. , Petterson, K. , Kim, S.-E. , Eloot, K. , Gietz, U. , Schiller, P. , and Rung, T. , 2015, " Experimental and Numerical Investigations on Flow Characteristics of KVLCC2 at 30° Drift Angle," Fifth World Maritime Technology Conference, Providence, RI, Nov. 3–7.

Bhushan, S., Yoon, H, Stern, F, Guilmineau, E., Visonneau, M., Toxopeus, S., Simonsen, C., Aram, S., Kim, S.-E. and Grigoropoulos, G., (2019) "Assessment of CFD for Surface Combatant 5415 at Straight Ahead and Static Drift b=20o," ASME JFE.

Brandt, A., Scorpio, S. M., Ericson, E. A., and Schemm, C. E., (2004) "Hydrodynamic Wakes of Surface Penetrating Structures," 25th Symposium on Naval Hydrodynamics, St. John's, Newfoundland and Labrador, CANADA, 8-13 August.

Broglia, R., Zaghi, S., Campana, E F, Dogan, T., Sadat-Hosseini, H. Stern, F., Queutey, P., Visonneau, M., Milanov, E., Assessment of Computational Fluid Dynamics Capabilities for the Prediction of Three-Dimensional Separated Flows: The DELFT 372 Catamaran in Static Drift Conditions, Journal of fluids engineering. , 2019, Vol.141(9), p.091105

Drazen, D., Fullerton, A., Fu, T., Beale, K., S'Shea, T., Brucker, A., Dommermuth, D., Wyatt, D., Bhushan, S., Carrica, P., Stern, F., "A comparison of model-scale experimental measurements and computational predictions for a large transom-stern wave," 28th Symposium Naval Hydrodynamics, Pasadena, CA, 12 – 17 September 2010.

Falgout, R.D., Jones, J.E. and Yang, U.M. (2006). "Numerical solution of partial differential equations on parallel computers," Berlin: Springer.

Frederick Stern, (2016) "Integrated High-Fidelity Validation Experiments and LES for a Surface-Piercing Truncated Cylinder for Sub- and Critical Reynolds and Froude Numbers," AVT-246: Progress and Challenges in Validation Testing for CFD, Avila, Spain, 26-28 September.

Koo, B., Yang, J., and Stern, F. (2014). "Reynolds and froude number effect on the flow past an interface-piercing circular cylinder," Int. J. of Naval Architecture and Ocean Engineering, Vol. 6, No. 3, pp. 529–561.

Longo, J., Huang, H.P., and Stern, F. (1998). "Solid-fluid juncture boundary layer and wake," Experiments in Fluids, Vol. 25, Issue 4, pp. 283–297.

NATO STO, (2017), "Reliable Prediction of Separated Flow Onset and Progression for Air and Sea Vehicles," STO Technical Report TR-AVT-183

Simonsen, C., Otzen, J., Quadvlieg, F., and Stern, F., (2017), "Proceedings SIMMAN 2014 Workshop," Copenhagen, Denmark, 8-10 December 2014.

Stern, F., Choi, J.E., and Hwang, W.S., "Effects of Waves on the Wake of a Surface-Piercing Flat Plate: Experiment and Theory," Journal of Ship Research, Vol. 37, No. 2, June 1993, pp. 102 – 118.

Stern, F.; Wilson, R.V.; Coleman, H.; and Paterson, E. "Comprehensive Approach to Verification and Validation

of CFD Simulations-Part 1: Methodology and procedures," ASME Journal of Fluids Engineering, 123, 4, July 2001, pp. 793–802.

Xing, T., and Stern, F., "Factors of Safety for Richardson Extrapolation," ASME J. Fluids Eng., 132, 6, June 2010, pp. 061403.

Stern, F., Agdrup, K., Kim, SY, Hochbaum, AC, Rhee, KP, Quadvlieg, F. (2011), Experience from SIMMAN 2008—the first workshop on verification and validation of ship maneuvering simulation methods, Journal of Ship Research 55 (2), 135-147

Suh, J., Yang, J. and Stern, F. (2011). "The effect of air-water interface on the vortex shedding from a vertical circular cylinder," J. of Fluids and Structures, Vol. 27, Issue 1, pp. 1–22.

Wang, Z., Suh, J., Yang, J., and Stern, F. (2012a). "Sharp interface LES of breaking waves by an interface piercing body in orthogonal curvilinear coordinates," 50th AIAA Paper.

Wang, Z., Yang, J., and Stern, F. (2009). "A coupled level set and volume of fluid method for 3D sharp interface simulation of plunging breaking waves," Int. J. of Multiphase Flow, Vol. 35, Issue 3, pp. 227–246.

Wang, Z., Yang, J., and Stern, F. (2012b). "A new volume of fluid method with constructed distance function on general structured grid," J. of Computational Physics, Vol. 231, Issue 9, pp. 3703–3722.

Wang, Z., Yang, J., and Stern, F. (2012c). "A simple and conservative operator-splitting semi-Lagrangian VOF advection scheme," J. of Computational Physics, Vol. 231, Issue 15, pp. 4981–4992.

Wang, Z., Yang, J., and Stern, F., "Numerical Simulations of wave breakings around a wedge-shaped bow," 28th Symposium Naval Hydrodynamics, Pasadena, Calif., 2010. Drazen et al., 2010

Xing, T., Kandasamy, M., and Stern, F. (2007). "Unsteady free-surface wave-induced separation: analysis of turbulent structures using detached eddy simulation and single-phase level set," J. of Turbulence, Vol. 8, No. 44, pp. 1–35.

Yang, J. and Stern, F. (2009). "Sharp interface immersed-boundary/level-set method for wave-body interactions," J. of Computational Physics, Vol. 228, Issue 17, pp. 6590–6616.

Yang, J., Bhushan, S., Suh, J., Wang, Z., Koo, B., Sakamoto, N., Xing, T. and Stern, F. (2008). "Large-eddy simulation of ship flows with wall-layer models on Cartesian grids," 27th Symposium on Naval Hydrodynamics, Seoul, Korea.

Yeon, S., Yang, J., and Stern, F. (2016). "Large-eddy simulation of the flow past a circular cylinder at sub- to super-critical Reynolds numbers," Applied Ocean Research, Vol. 59, pp. 663–675.

Yoon, H. and Stern, F., Phase-averaged TPIV Measurements for Surface Combatant 5415 in Pure Sway Maneuver: Experimental Setup, UA and Preliminary Results," 30th ATTC, Bethesda, MD, October 2017.

Yoon, H., Gui, L., Bhushan, S., and Stern, F. (2014). "Tomographic PIV measurements for a surface combatant at straight ahead and static drift conditions," 30th Symposium on Naval Hydrodynamics, Hobart, Australia.

Yoon, H., Simonsen, CD, Benedetti, L., Longo, J., Toda, Y., Stern, F., Benchmark CFD validation data for surface combatant 5415 in PMM maneuvers–Part I: Force/moment/motion measurements, Ocean Engineering 109, 705-734, November 2015a.

Yoon, Hyunse, Longo, Joseph, Toda, Yasuyuki, and Stern, Frederick, "Benchmark CFD Validation Data for Surface Combatant 5415 in PMM Maneuvers – Part 2: Phase-averaged SPIV flow field measurements," Ocean Engineering, 109, pp. 735-750, November 2015b.

Yoon, S.-H., Kim, D.-H., Sadat-Hosseini, H., Yang J., and Stern, F. (2016). "High-fidelity CFD simulation of wave run-up for single/multiple surface-piercing cylinders in regular head waves," Applied Ocean Research, Vol. 59, pp. 687–708.

Yoon, S.-H., Yoon, H., Stern, F., (2019a), "Integrated high-fidelity validation experiments and LES for a surface-piercing truncated cylinder for sub and critical Reynolds and Froude numbers," IIHR Report #xxx.

Yoon, S.-H., Sanada, Y., Wang, Z., Yoneda, S. and Stern, F. (2019b), "Effects of sway motion on surface-piercing truncated cylinder for sub-critical Reynolds and Froude numbers: experiments and LES," IIHR technical report #xxx

Table 2-1. 5512 model main particulars.

Parameter	Units	5512	Full scale
Linear scale ratio	-	46.6	1
Length L	m	3.048	142.04
Beam B	m	0.405	18.87
Draft T	m	0.132	6.15
Wetted surface area BH S_w	m^2	1.378	2977
Wetted surface area BK S_w	m^2	1.443	3168
Block coefficient C_B	-	0.506	0.506
Metacentric height GM	m	0.043	2.00
Longitudinal center of gravity LCG[a]	m	1.536	71.58
Vertical center of gravity VCG[b]	m	0.030	1.40
Roll radius of gyration k_{44}=0.39B	m	0.158	7.36
Natural roll period	s	1.54	10.51[c]

a: Measured from origin; b: measured from waterline; c: from Bishop (1983)

Bilge Keel Placement			
Station	X	Y	Z
Start	1136.1	±135.1	-85.0
8	1218.9	±138.2	-89.8
9	1371.1	±142.2	-97.5
10	1523.5	±144.5	-102.3
11	1675.9	±143.8	-104.6
12	1828.3	±141.0	-102.5
13	1980.7	±137.7	-95.4
14	2133.1	±133.1	-85.3
End	2151.1	±132.6	-83.7

Table 2-2. Test conditions.

Parameter	Symbol	Unit	Hyunse et al. (2015 and 2017)		Present	
			Force/ moment	TPIV	Force/ moment	TPIV
Towing speed	U_C	m/s	1.531		1.534	
Froude number	$Fr = \frac{U_C}{\sqrt{gL}}$	-	0.28		0.28	
Reynolds number	$Re = \frac{U_C L}{\nu}$	-	4.65×10^6		4.458×10^6 - 4.514×10^6	
Water temperature	T_w	°C	20		18.2 – 18.7	
Sinkage	σ	L	1.92×10^{-3}			
[1)]Trim	τ	°	-0.136			
Max. drift angle	β_{max}	°	2, 4, 10	10	2, 4, 10	10
Max. sway velocity	v_{max}	U_C	0.035, 0.070, 0.176	0.176	0.035, 0.070, 0.175	0.175

[1)]Positive bow up.

Table 2-3. PMM sway amplitude and frequency values.

Parameter	Hyunse et al. (2015 and 2017)		Present	
	Forces/moment measurement	TPIV measurement	Forces/moment measurement	
				4DPTV uniform flow
y_{max} (L)	0.021, 0.042, 0.104	0.087	0.021, 0.042, 0.105	0.086
f (Hz)	0.134	0.162	0.134	0.162
ω (rad/s)	0.848	1.018	0.848	1.018

Table 2-4. Surge X comparison between present and Hyunse (2007)

June 2019 (D_1, Tw=18.2 °C)				March 2007 (D_2, Tw= 12.8 - 13.3 °C)		Mean	(D_1-D_2) %D_m
Fr	Number of runs	X [-] × 10^3	SD%Mean (X [-] × 10^3) [%]	Fr	X [-] × 10^3	D_m=(D_1+D_2)/2	
0.140	3	-1.615E+01	0.96	0.138	-1.680E+01	-1.647E+01	-3.96
0.281	3	-1.621E+01	0.49	0.280	-1.600E+01	-1.610E+01	1.30
0.409	5	-2.114E+01	0.30	0.410	-2.030E+01	-2.072E+01	4.04

Table 2-5. Static drift data comparison between present and Hyunse (2007)

β [°]	June 2019 (Tw=18.2 °C)								
	Number of runs	Mean				SD%Mean			
		X [-] × 10^3	Y [-] × 10^3	K [-] × 10^3	N [-] × 10^3	X [-] × 10^3	Y [-] × 10^3	K [-] × 10^3	N [-] × 10^3
0	5	-1.621E+01	4.128E-01	7.339E-02	-8.667E-01	0.49	18.22	5.82	56.93
10	3	-1.989E+01	5.381E+01	-5.143E+00	2.447E+01	1.13	3.10	2.04	4.64
20	3	-2.996E+01	1.423E+02	-1.375E+01	5.426E+01	1.15	0.37	0.63	2.13
-10	3	-1.966E+01	-5.360E+01	5.438E+00	-2.689E+01	4.49	2.81	0.82	16.69
-20	3	-3.049E+01	-1.415E+02	1.394E+01	-5.535E+01	1.27	0.74	0.38	2.30

β [°]	June 2019 (D_1, Tw=18.2 °C)			March 2007 (D_2, Tw= 12.8 - 13.3 °C)			(D_1-D_2) %D_m		
	X [-] × 10^3	Y [-] × 10^3	N [-] × 10^3	X [-] × 10^3	Y [-] × 10^3	N [-] × 10^3	X [-] × 10^3	Y [-] × 10^3	N [-] × 10^3
0	-1.621E+01	4.128E-01	-8.667E-01	-1.600E+01	3.200E+00	1.000E+00	1.30	-154.30	-2800.03
10	-1.989E+01	5.381E+01	2.447E+01	-1.880E+01	5.430E+01	2.620E+01	5.66	-0.91	-6.82
20	-2.996E+01	1.423E+02	5.426E+01	-2.750E+01	1.436E+02	5.530E+01	8.57	-0.98	-1.90
-10	-1.966E+01	-5.360E+01	-2.689E+01						
-20	-3.049E+01	-1.415E+02	-5.535E+01						

Table 2-6. Comparison between positive and negative β

β[°]	Symmetry of static drift (positive β(r^+) vs negative β(r^-), (r^+ - r^-)%r_m, r_m = (r^+ + r^-)/2			
	X [-]	Y [-]	K [-]	N [-]
10	-1.17	-0.38	5.57	9.39
20	1.73	-0.51	1.38	1.99

Table 2-7 Summary of FS sine and cosine coefficients of pure sway X, Y and N

f[Hz]	y_{max}/L	v_{max}/U_C	$\dot{v}_{max}L/U_C^2$	Number of runs	Mean		SD%Mean	
					$X_0\times 10^3$	$X_{C2}\times 10^3$	$X_0\times 10^3$	$X_{C2}\times 10^3$
0.134	0.021	3.519E-02	5.886E-02	5	-1.514E+01	9.255E-01	15.3	98.2
0.134	0.042	7.008E-02	1.172E-01	5	-1.563E+01	8.908E-03	6.1	10358.5
0.162	0.086	1.742E-01	3.522E-01	13	-1.704E+01	8.612E-01	25.8	94.3
0.134	0.105	1.750E-01	2.928E-01	13	-1.842E+01	3.365E+00	19.2	22.9

f[Hz]	y_{max}/L	v_{max}/U_C	$\dot{v}_{max}L/U_C^2$	Number of runs	$Y_{C1}\times 10^3$	$Y_{C3}\times 10^3$	$Y_{S1}\times 10^3$	SD%Mean		
								$Y_{C1}\times 10^3$	$Y_{C3}\times 10^3$	$Y_{S1}\times 10^3$
0.134	0.021	3.519E-02	5.886E-02	5	7.637E+00	5.385E-01	-5.614E+00	0.16	0.97	-0.55
0.134	0.042	7.008E-02	1.172E-01	5	1.704E+01	1.043E+00	-1.087E+01	0.04	0.22	-0.08
0.162	0.086	1.742E-01	3.522E-01	13	5.256E+01	2.523E+00	-3.832E+01	0.04	0.42	-0.02
0.134	0.105	1.750E-01	2.928E-01	13	5.051E+01	2.345E+00	-3.095E+01	0.02	0.37	-0.04
f[Hz]	**y_{max}/L**	**v_{max}/U_C**	**$\dot{v}_{max}L/U_C^2$**	**Number of runs**	**$N_{C1}\times 10^3$**	**$N_{C3}\times 10^3$**	**$N_{S1}\times 10^3$**	**SD%Mean**		
								$N_{C1}\times 10^3$	$N_{C3}\times 10^3$	$N_{S1}\times 10^3$
0.134	0.021	3.519E-02	5.886E-02	5	5.022E+00	-5.348E-02	-8.274E-01	0.03	-2.25	-0.11
0.134	0.042	7.008E-02	1.172E-01	5	1.022E+01	4.348E-01	-1.964E+00	0.01	0.21	-0.07
0.162	0.086	1.742E-01	3.522E-01	13	2.660E+01	3.792E-01	-4.208E+00	0.01	0.11	-0.05
0.134	0.105	1.750E-01	2.928E-01	13	2.621E+01	6.236E-02	-3.409E+00	0.01	1.28	-0.07

Table 2-8 FS coefficients comparison between present and Hyunse (2015) (β_{max}=10°, f=0.134 Hz)

June 2019 (D_1)			2015 (D_2)			(D_1-D_2) %D_m		
$X_0\times 10^3$	$X_{C2}\times 10^3$		$X_0\times 10^3$	$X_{C2}\times 10^3$		$X_0\times 10^3$	$X_{C2}\times 10^3$	
-2.344E+01	3.365E+00		-1.778E+01	8.470E-01		27.46	119.56	
$Y_{C1}\times 10^3$	$Y_{C3}\times 10^3$	$Y_{S1}\times 10^3$	$Y_{C1}\times 10^3$	$Y_{C3}\times 10^3$	$Y_{S1}\times 10^3$	$Y_{C1}\times 10^3$	$Y_{C3}\times 10^3$	$Y_{S1}\times 10^3$
5.051E+01	2.345E+00	-3.095E+01	5.630E+01	1.914E+00	-2.968E+01	-10.83	20.23	4.21
$N_{C1}\times 10^3$	$N_{C3}\times 10^3$	$N_{S1}\times 10^3$	$N_{C1}\times 10^3$	$N_{C3}\times 10^3$	$N_{S1}\times 10^3$	$N_{C1}\times 10^3$	$N_{C3}\times 10^3$	$N_{S1}\times 10^3$
2.621E+01	6.236E-02	-3.409E+00	2.857E+01	3.250E-01	-2.265E+00	-8.62	-135.60	40.31

Table 2-9 FS coefficients comparison between present and Hyunse (2017) (β_{max}=10°, f=0.134 Hz)

June 2019 (D_1)			2017 (D_2)			(D_1-D_2) %D_m		
$X_0\times 10^3$	$X_{C2}\times 10^3$		$X_0\times 10^3$	$X_{C2}\times 10^3$		$X_0\times 10^3$	$X_{C2}\times 10^3$	
-2.344E+01	3.365E+00		-1.867E+01	3.000E-03		22.63	199.64	
$Y_{C1}\times 10^3$	$Y_{C3}\times 10^3$	$Y_{S1}\times 10^3$	$Y_{C1}\times 10^3$	$Y_{C3}\times 10^3$	$Y_{S1}\times 10^3$	$Y_{C1}\times 10^3$	$Y_{C3}\times 10^3$	$Y_{S1}\times 10^3$
5.051E+01	2.345E+00	-3.095E+01	5.270E+01	2.845E+00	-3.075E+01	-4.23	-19.27	0.64
$N_{C1}\times 10^3$	$N_{C3}\times 10^3$	$N_{S1}\times 10^3$	$N_{C1}\times 10^3$	$N_{C3}\times 10^3$	$N_{S1}\times 10^3$	$N_{C1}\times 10^3$	$N_{C3}\times 10^3$	$N_{S1}\times 10^3$
2.621E+01	6.236E-02	-3.409E+00	2.647E+01	8.150E-01	-2.491E+00	-0.99	-171.57	31.10

Table 2-10 Summary of uniform flow measurements for 6 different carriage speeds

Motor output [%]	Number of runs	Carriage speed (U_C) (D1) [m/s]	4DPTV |U| (D2) [m/s]	|D2-D1|%Dm	Tan^{-1}(v/u) [°]	Tan^{-1}(w/u) [°]
10.00	2	0.331	0.335	1.11	1.40	-0.34
20.00	1	0.663	0.666	0.56	1.31	-0.33
30.00	2	0.993	0.997	0.38	1.32	-0.33
40.00	1	1.324	1.332	0.59	1.20	-0.46
46.38	3	1.535	1.538	0.17	1.21	-0.46
50.00	1	1.655	1.645	0.61	1.23	-0.47
Average				**0.57**	**1.28**	**-0.40**

Table 2-11 Summary of static drift uniform flow measurements (β=0°, ±10° and ±20°)

β [°]	Motor output [%]	Number of runs	Carriage speed (U_C) (D1) [m/s]	4DPTV |U| (D2) [m/s]	|D2-D1|%Dm	Tan^{-1}(v/u) [°]	Tan^{-1}(w/u) [°]	β + Tan^{-1}(v/u) [°]
20	46.38	2	1.535	1.552	1.04	-19.17	-0.80	0.83
10	46.38	2	1.536	1.539	0.21	-8.56	-0.71	1.44
0	46.38	3	1.535	1.538	0.17	1.21	-0.44	1.21
-10	46.38	2	1.536	1.531	0.28	10.46	-0.73	0.46
-20	46.38	2	1.531	1.524	0.44	20.94	-0.45	0.94
Average					**0.43**			**0.97**

Table 2-12 Summary of pure sway uniform flow measurements (f=0.162 Hz, v_{max}=0.175, Uc=1.535 m/s)

Run #	4DPTV U_0 [m/s]	$Tan^{-1}(v_0/u_0)$ [°]	$Tan^{-1}(w_0/u_0)$ [°]	v_1(4DPTV) (D_1) [m/s]	v_{sway1} (D_2)[m/s]	(D_1-D_2)%D_2
1	1.551	-1.141	-0.062	0.248	0.269	-7.853
2	1.550	-1.202	-0.016	0.250	0.269	-7.212
3	1.555	-1.192	-0.004	0.247	0.269	-8.165
Average	**1.552**	**-1.178**	**-0.027**	**0.248**	**0.269**	**-7.743**

Table 3-1 Test matrix of pure sway experiment*

#	Re	Fr	U [m/s]	T [°C]	A/D	f_e/f_o	f_e [Hz]	λ/D	$\frac{V_{max}}{U}$ [%]	α_{max} [°]	St	Data rate [Hz]	Number of runs** (Forward /Backward)	Time period per run [s]	# of cycles per run***
1						**0.75**	**0.078**	**7.84**	**40.1**	**21.8**					**15**
2						0.875	0.091	6.72	46.7	25.0					18
3	27,000	0.093	0.130	21.7	**0.5**	**1**	**0.104**	**5.88**	**53.4**	**28.1**	**0.17**	**2000**	**3/3**	**0 ~ 200**	**20**
4						1.125	0.117	5.23	60.1	31.0					23
5						**1.25**	**0.130**	**4.71**	**66.8**	**33.7**					**26**
6						**0.75**	**0.333**	**7.84**	**40.1**	**21.8**					**16**
7						0.875	0.389	6.72	46.7	25.0					19
8	123,000	0.423	0.592	22.2	**0.5**	**1**	**0.444**	**5.88**	**53.4**	**28.1**	**0.17**	**2000**	**3/3**	**0 ~ 50**	**22**
9						1.125	0.500	5.23	60.1	31.0					25
10						**1.25**	**0.555**	**4.71**	**66.8**	**33.7**					**27**
11						0.75	0.078	7.84	40.1	21.8					15
12						0.875	0.091	6.72	46.7	25.0					18
13	27,000	0.093	0.130	21.7	0.25	1	0.104	5.88	53.4	28.1	0.17	2000	3/3	0 ~ 200	20
14						1.125	0.117	5.23	60.1	31.0					23
15						1.25	0.130	4.71	66.8	33.7					26
16						0.75	0.333	7.84	40.1	21.8					16
17						0.875	0.389	6.72	46.7	25.0					19
18	123,000	0.423	0.592	22.2	0.25	1	0.444	5.88	53.4	28.1	0.17	2000	3/3	0 ~ 50	22
19						1.125	0.500	5.23	60.1	31.0					25
20						1.25	0.555	4.71	66.8	33.7					27

* All experiments are performed for truncated cylinder with aspect ratio AR=4
** Total 120 data files: 20 cases * 6 runs = 120
*** Cycles = cylinder motion cycles

Table 3-2 Summary of pure sway LES

		Re, Fr	A/D	f_e/f_o	Grid					Y^+	Status	Numer. scheme	Domain size			AR L/D	Analyzed shedding cycles	Estimated computing time [weeks]
					N_r	N_θ	N_z	Total					Inlet	Outlet	Side			
Overset grid	Present sub-critical	27,000 0.8	0.5	0.75	64	64	40	0.5M	C	8.2	Done	Semi-L + WENO5	20D	20D	20D	8	10	0.2
				1.00													10	0.2
				1.25													10	0.2
	Present sub-critical	27,000 0.1		0.75	96	96	50	0.7M	C	7.5	Done	Semi-L + WENO5	20D	20D	20D	4T	10	0.2
				1.00													10	0.2
				1.25													10	0.2
	Present sub-critical	123,000 0.5	0.5	0.75	64	128	80	1.6M	C	3.0	Done	Semi-L + WENO5	20D	20D	20D	4T	10	0.7
				1.00														
				1.25														
				0.75	128	256	160	6.8M	M	1.6	Done						10*	7
				1.00														
				1.25														
				0.75	256	256	160	13M	F	0.7	Done						10*	18
				1.00														
				1.25														

Table 3-3 Grid uncertainty analysis of integral variables: pure sway at (Re, Fr)=(27,000, 0.1) and (123,000, 0.5)

Parameter			S_1	ε_{21}	R_G	P_G	$P=P_G/P_{th}$	$U_I\%S_1$	$U_I/\lvert\varepsilon_{21}\rvert$	$U_I\%U_G$	$U_{FS}\%S_1$
f_e/f_K=0.75	C_{D1}	MC	0.1710	-0.003	0.1111	2.20	0.439	0.022	0.0330	61.78	1.02
	ϕ_D	MC	207.7	0.400	0.0067	6.90	1.380	-194.355	0.4335	104.43	0.007
	C_{D0}	MC	1.110	-0.040	0.2500	0.61	0.122	4.575	1.7383	38.85	16.1
	C_{L1}	MC	0.440	-0.025	0.1613	1.49	0.297	0.269	0.1236	62.78	6.9
	ϕ_L	MC	118.7	-10.90	0.0700	3.04	0.607	-130.324	3.0290	30.89	0.81
f_e/f_K=1.00	C_{D1}	MC	0.2780	-0.0005	0.0909	2.57	0.513	0.022	0.1230	30.04	0.07
	ϕ_D	MC	1.6700	1.2800	0.1891	1.17	0.235	16.141	0.2106	11.76	0.64
	C_{D0}	MC	1.320	-0.0300	0.2308	0.77	0.155	0.956	0.4208	12.86	7.43
	C_{L1}	MC	1.250	-0.0400	0.1739	1.34	0.268	1.357	0.4240	29.20	4.65
	ϕ_L	MC	-29.34	9.7800	0.2994	0.23	0.046	-13.102	0.3931	2.82	37.88
f_e/f_K=1.25	C_{D1}	MC	0.3040	-0.0020	0.0217	5.03	1.01	0.044	0.0250	4.31	0.04
	ϕ_D	MC	-0.093	-0.4170	0.0916	2.55	0.510	0.010	0.0500	75.64	0.048
	C_{D0}	MC	1.140	0.0300	0.2500	0.61	0.122	1.041	0.2888	6.45	11.77
	C_{L1}	MC	1.840	-0.0400	0.0571	3.39	0.679	0.362	0.0638	5.23	0.43
	ϕ_L	MC	-10.18	4.3800	0.2876	0.32	0.0631	0.232	0.0252	9.40	11.93

Table 3-4 Validation of integral variables: pure sway at (Re, Fr)=(27,000, 0.1) and (123,000, 0.5)

Re, Fr	A/D	f_e/f_o	C_{D1}			ϕ_D [°]			C_{D0}			C_{L1}			ϕ_L [°]		
			EFD	LES	E	EFD	LES	E*	EFD	LES	E	EFD	LES	E	EFD	LES	E*
27,000 0.1 (coarse)	0.5	0.75	0.080	0.173	-116	226.65	190	10.2	1.17	1.09	6.8	0.08	0.22	-175	180	220	-11.1
		1.00	0.168	0.303	-80.4	5.17	-15.7	5.8	1.44	1.38	4.2	1.76	0.63	64.2	2.24	-18.9	5.9
		1.25	0.389	0.314	19.3	11.58	-6.70	5.1	1.20	1.12	6.7	2.19	1.89	13.7	-6.12	3.98	-2.8
		Mean	**0.212**	**0.263**	**72.0**	**81.1**	**55.9**	**7.0**	**1.27**	**1.20**	**5.9**	**1.34**	**0.91**	**84.3**	**58.7**	**68.4**	**6.6**
123,000 0.5 (coarse)	0.5	0.75	0.089	0.141	-58.4	219.6	267.6	-13.3	1.20	0.9100	24.2	0.15	0.260	-73.3	197	-48.0	68.2
		1.00	0.252	0.273	-8.3	1.64	9.72	-2.2	1.37	1.16	15.3	1.99	0.98	50.8	-7.21	10.3	-4.9
		1.25	0.333	0.210	36.9	16.73	-5.06	6.1	1.16	1.29	-11.5	2.18	1.10	49.5	-21.9	8.43	-8.4
		Mean	**0.225**	**0.208**	**34.57**	**79.31**	**90.75**	**7.22**	**1.24**	**1.13**	**16.43**	**1.44**	**0.78**	**57.88**	**56.1**	**-9.76**	**27.2**
123,000 0.5 (medium)	0.5	0.75	0.089	0.168	-88.8	219.6	208.1	3.2	1.20	1.07	10.8	0.15	0.415	-177	197	107.8	24.9
		1.00	0.252	0.277	-9.9	1.64	2.95	-0.4	1.37	1.29	5.8	1.99	1.21	39.1	-7.21	-16.56	2.6
		1.25	0.333	0.302	9.3	16.73	-0.51	4.8	1.16	1.19	-2.6	2.18	1.80	17.6	-21.93	-4.80	-4.8
		Mean	**0.225**	**0.250**	**37.1**	**79.31**	**70.17**	**2.8**	**1.24**	**1.20**	**5.3**	**1.44**	**1.15**	**86.5**	**56.1**	**32.45**	**9.7**
123,000 0.5 (fine)	0.5	0.75	0.089	0.171	-92.1	219.6	207.7	3.3	1.20	1.11	7.5	0.15	0.440	-193.3	197	118.7	21.9
		1.00	0.252	0.278	-10.3	1.64	1.67	-0.01	1.37	1.32	3.6	1.99	1.25	37.2	-7.21	-30.34	6.4
		1.25	0.333	0.304	8.8	16.73	-0.093	4.7	1.16	1.13	2.5	2.18	1.84	15.5	-21.93	-10.81	-3.1
		Mean	**0.225**	**0.251**	**37.1**	**79.31**	**69.76**	**2.7**	**1.24**	**1.187**	**4.5**	**1.44**	**1.177**	**82.0**	**56.08**	**25.85**	**10.5**

E*=(D-S)%360°

Table 3-5 Vertical locations for four zones (free surface/free surface transition/bottom transition/bottom) and separation angles at three vertical locations for PIV measurement

	Stern (2016)		Straight ahead		fe/fo=0.75		fe/fo=1.00		fe/fo=1.25	
z_F	-0.5		-0.5		-1.0		-1.0		-1.5	
z_B	-3.5		-3.5		-3.5		-3.8		-3.8	
	Zone	θs [°]	Zone	θs [°]	Zone	θs [°]	Zone	θs [°]	Zone	θs [°]
at z=-0.75	Free surface transition	79.0	Free surface transition	80.2	Free surface	110	Free surface	133	Free surface	148
at z=-2.00	Quasi-2D	78.9	Quasi-2D	78.9	Quasi-2D	101	Quasi-2D	117	Free surface transition	111
at z=-3.50	Bottom	84.4	Bottom	83.0	Bottom	106	Bottom transition	115	Bottom transition	108

Table 3-6 Separation angle and shear layer angle on free surface

Case	Separation angle and difference between straight ahead and sway			Shear layer angle on free surface			Angle between streamwise and transverse velocity	α_{in} - $\lvert\Delta\theta s\rvert$ [°]	α_{in} - $\Delta\alpha_{fs}$ [°]
	θs [°]		$\Delta\theta s = \theta s_i - \theta s_0$ [°]	α_{fs} [°]		$\Delta\alpha_{fs} = \alpha_{fsi} - \alpha_{fs0}$ [°]	α_{in} [°]		
NATO (F)	θs_0	74.0	-	α_{fs0}	60.5	-	0	-	-
Straight ahead	θs_0	74.4	-	α_{fs0}	60.0	-	0	-	-
fe/fo=0.75	θs_1	65.6	-8.8	α_{fs1}	73.9	13.9	14.3	5.5	0.4
fe/fo=1.00	θs_2	50.6	-23.7	α_{fs2}	78.9	18.9	18.8	-4.9	-0.1
fe/fo=1.25	θs_3	18.4	-56.0	α_{fs3}	87.1	27.1	23.0	-33.0	-4.1

Table 3-7 Bottom vortices angle

Case	Bottom vortices angle			α_{in} - $\Delta\alpha_b$ [°]
	α_b [°]		$\Delta\alpha_b = \alpha_{bi} - \alpha_{b0}$ [°]	
NATO (F)	α_{b0}	21.6	-	-
Straight ahead	α_{b0}	24.3	-	-
fe/fo=0.75	α_{b1}	33.6	9.2	5.1
fe/fo=1.00	α_{b2}	38.4	14.0	4.7
fe/fo=1.25	α_{b3}	44.3	20.0	3.1

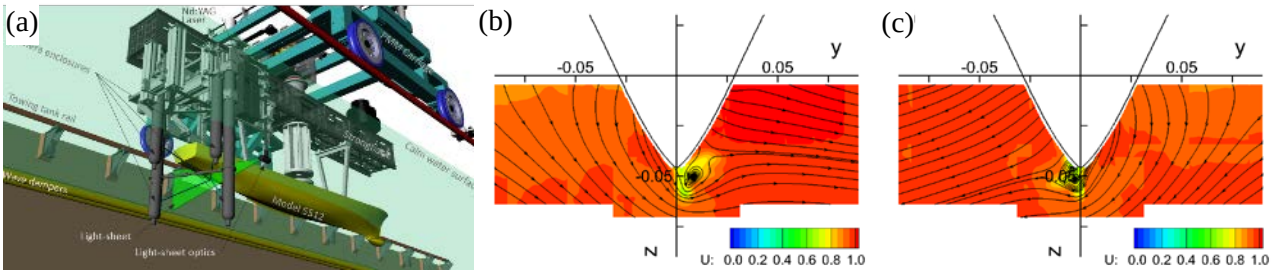

Figure 2-1 5415 pure sway towing tank PMM towed TPIV. Integrated URANS and DES via NATO-AVT 253: a graphical rendering (a) and contours of U with VW-streamlines at x=0.12 for (b) γ=0°, (c) γ=135°

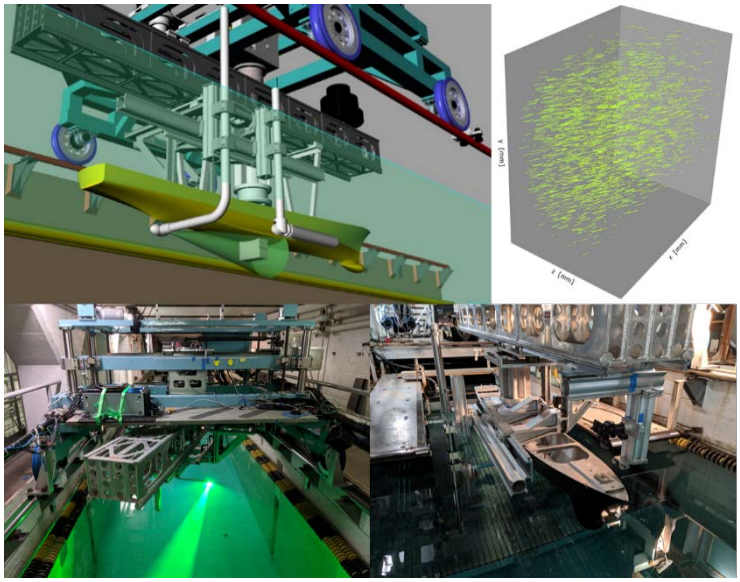

Figure 2-2 5415 pure sway 4D-PTV

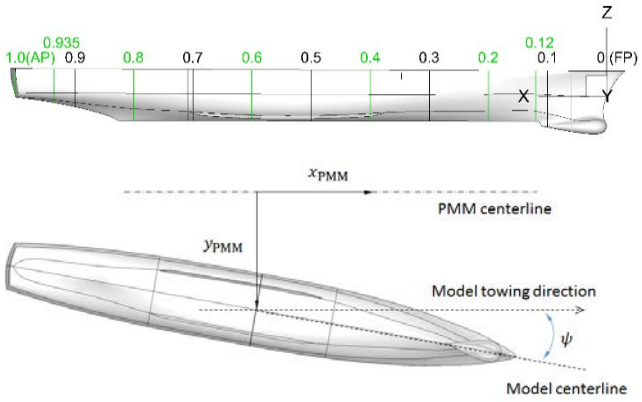

Figure 2-3. Ship-fixed xyz-coordinate system (top) and PMM-fixed $x_{PMM}y_{PMM}$-coordinate system (bottom).

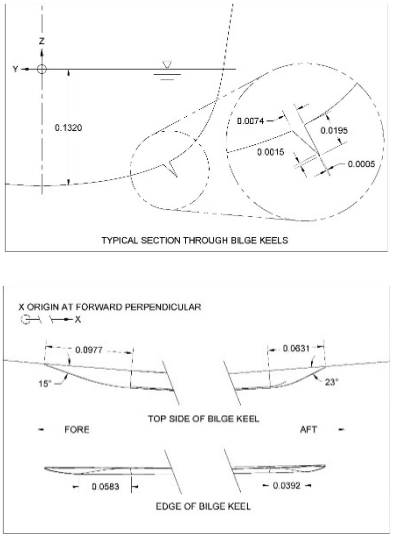

Figure 2-4 Details bilge keel geometry and location and photo of the refurbished 5512 model.

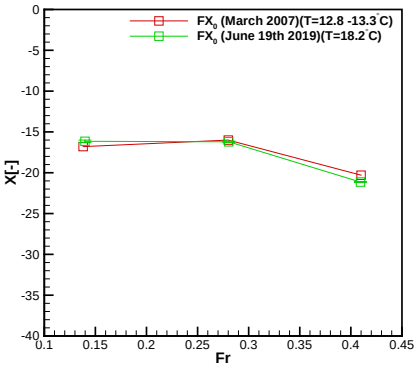

Figure 2-5. Surge X in calm water at β = 0 °(FX0, Fr=0.140, 0.281 and 0.409).

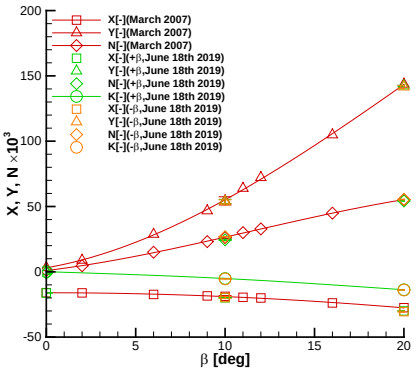

Figure 2-6. Surge X and sway Y forces and roll K and yaw N moments at for β = 0°, 10°, and 20° (FX0, Fr=0.280).

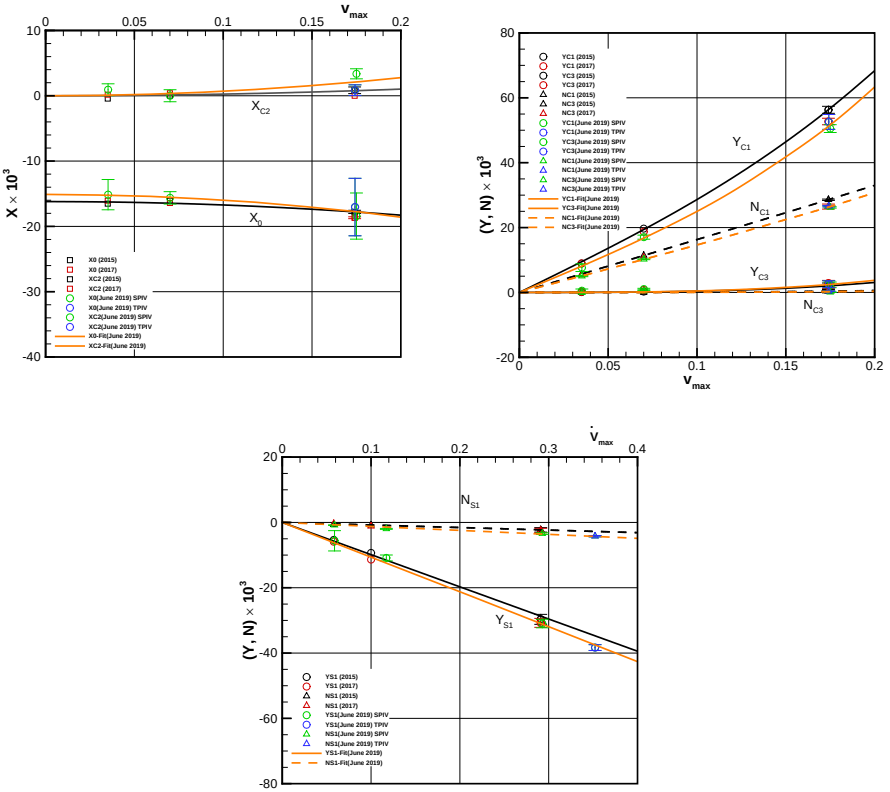

Figure 2-7 FS sine and cosine coefficients of pure sway *X*, *Y* and *N*.

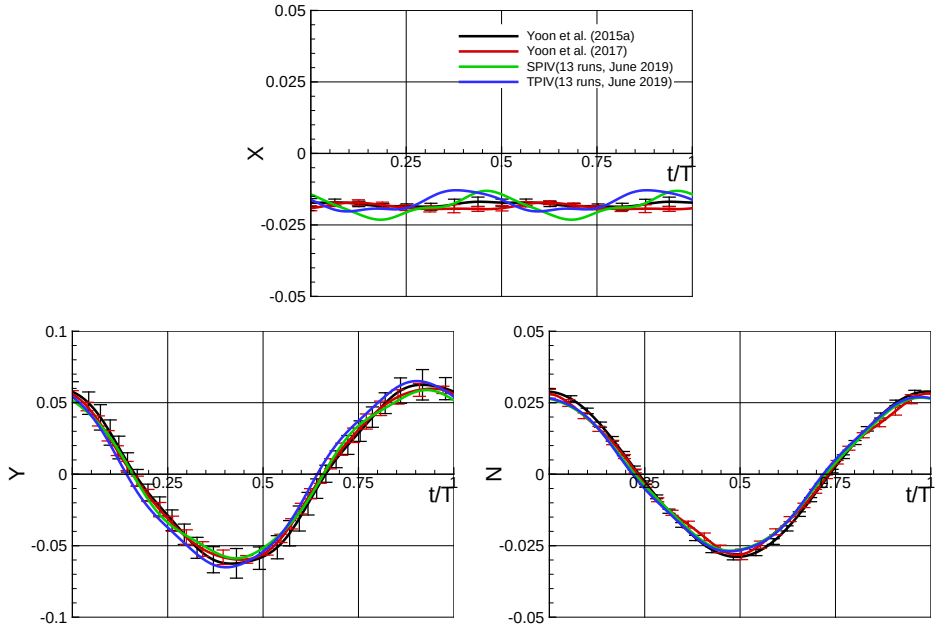

Figure 2-8 Reconstructed time-histories of (X, Y, N) for βmax=20° (2015, 2017 and present)

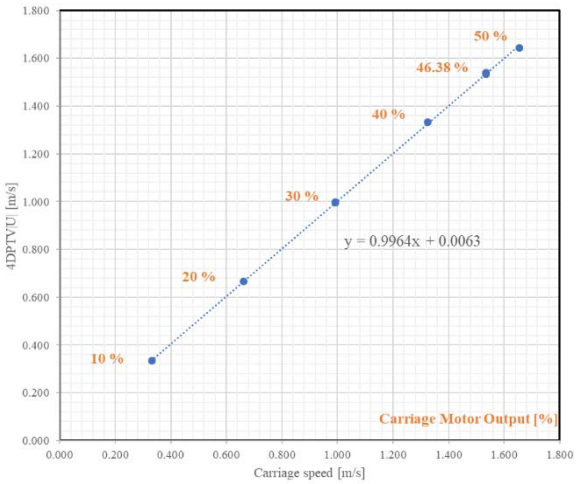

Figure 2-9 Comparison between carriage speed and whole volume mean velocity by 4DPTV

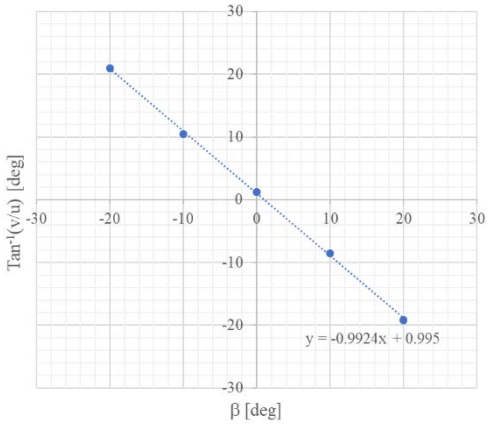

Figure 2-10 Relationship between static drift angle β and whole volume mean Tan-1(v/u)

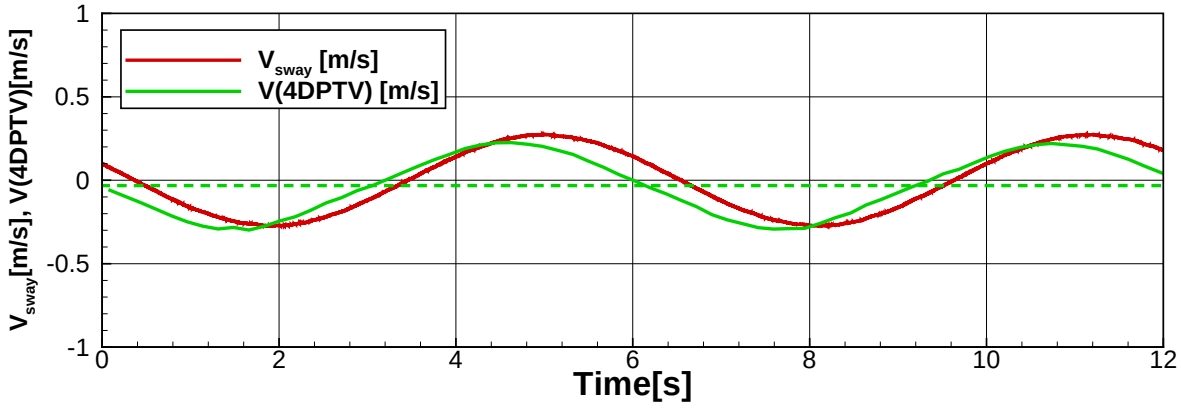

Figure 2-11 PMM sway velocity and whole volume mean velocity by 4DPTV under pure sway (f=0.162 Hz)

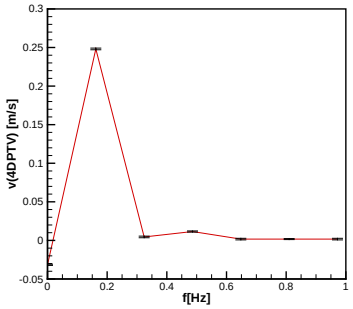

Figure 2-12 Harmonic amplitudes of whole volume mean sway velocity by 4DPTV

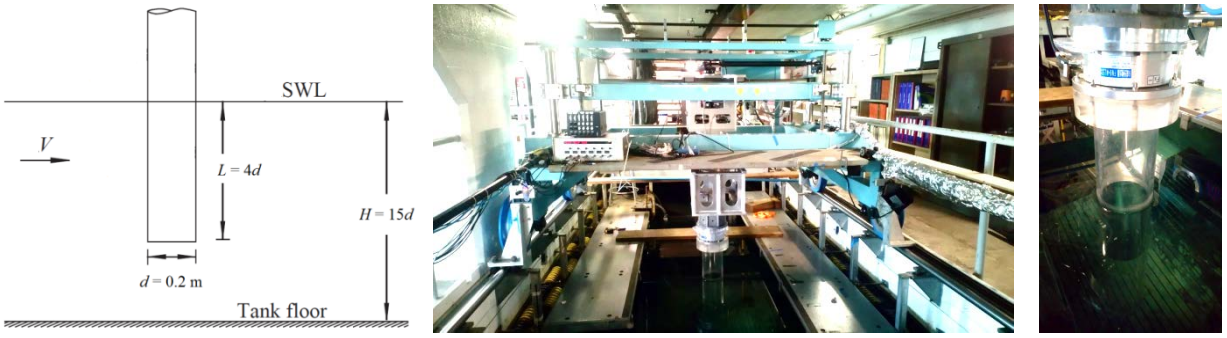

Figure 3-1 Schematics (left), PMM carriage (middle) and setup for surface piercing truncated cylinder (right)

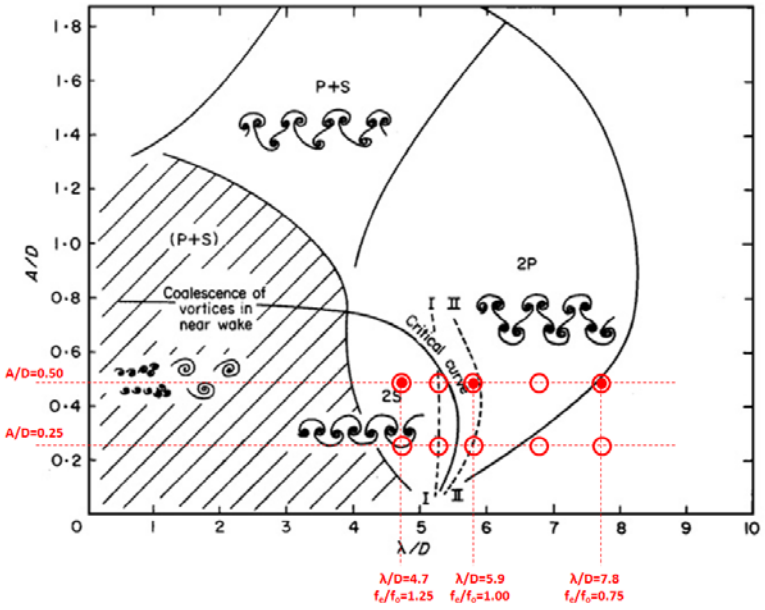

Figure 3-2 The map of regimes for vortex wake modes for controlled oscillating cylinder [Williamson and Roshko (1988), Williamson and Govardhan (2008)]; I, II are the curves where the forces on the body show a sharp "jump"; from Bishop and Hassan (1964). I is for wavelength decreasing and II is for wavelength increasing.

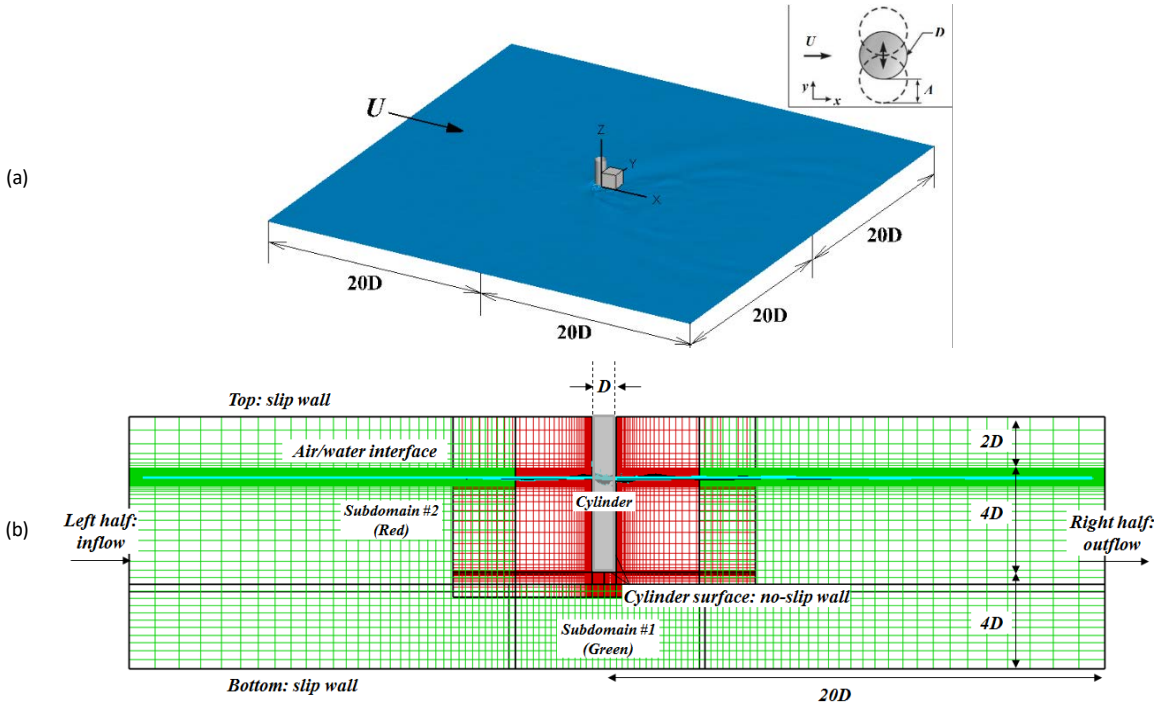

Figure 3-3 Schematic diagram of the computational domain, boundary conditions for truncated cylinder simulation with overset cylindrical grid for (Re, Fr) = (123K, 0.5): (a) three-dimensional view, (b) side view

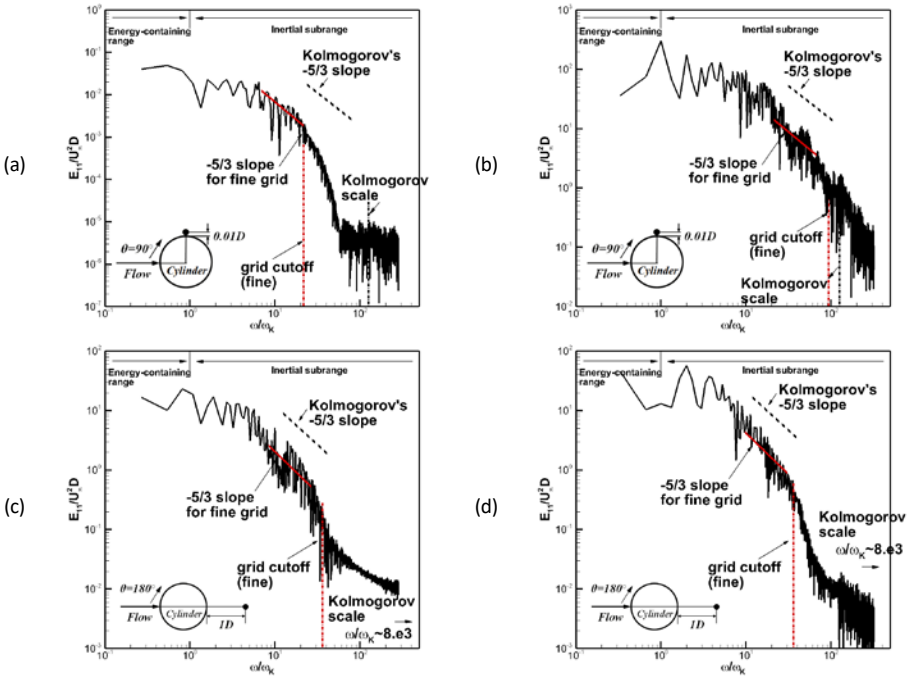

Figure 3-4 Turbulent kinetic energy spectra in the shear layer near the cylinder (0.01D from wall) and vortex formation region (1D away from wall, x=1.5): (left) straight ahead, (right) f_e/f_K=1.00

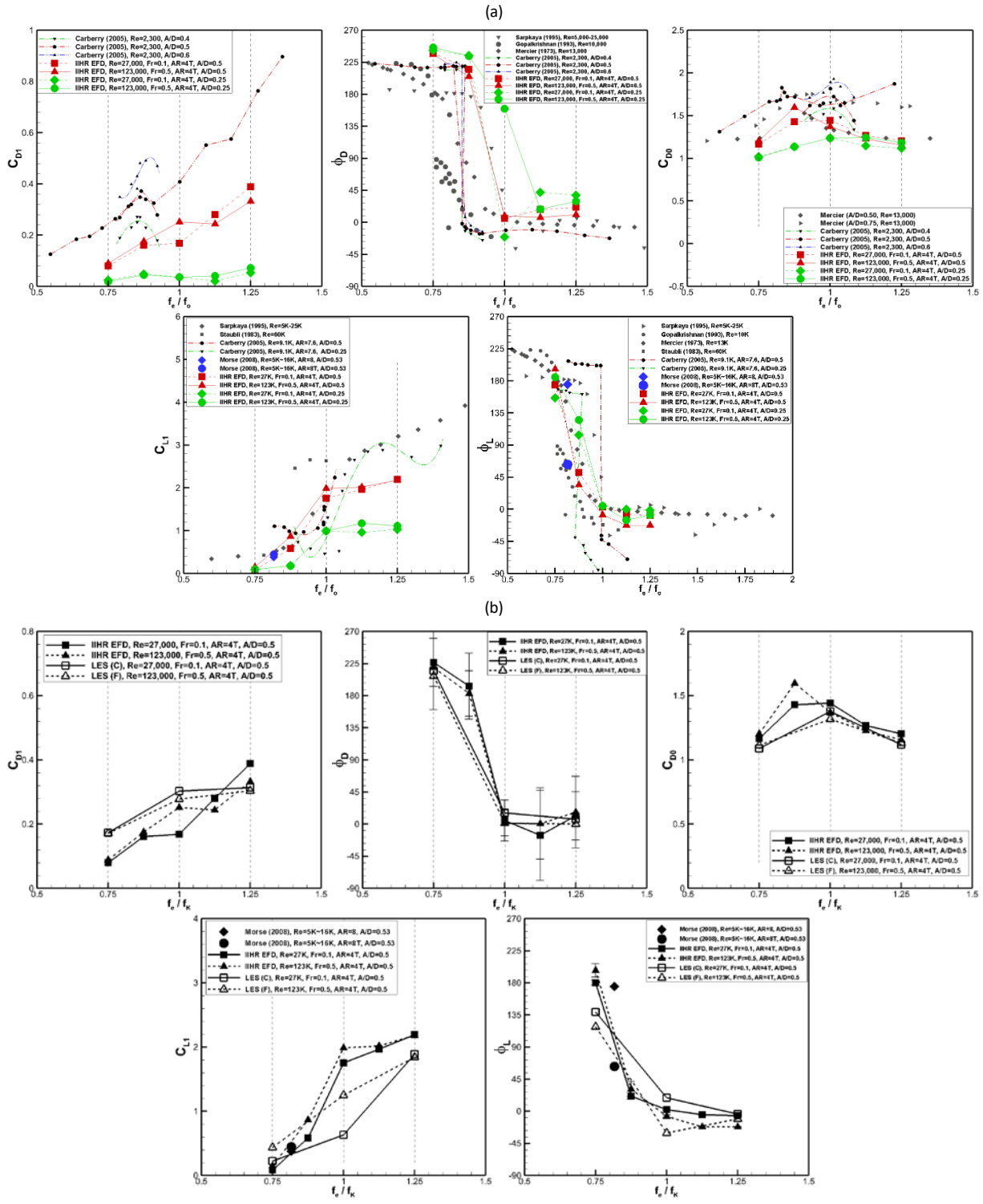

Figure 3-5 Comparisons with benchmark data for C_{D1}, Φ_D,C_{D0}, C_{L1} and Φ_L: (a) EFD vs. benchmark data, (b) EFD vs. LES

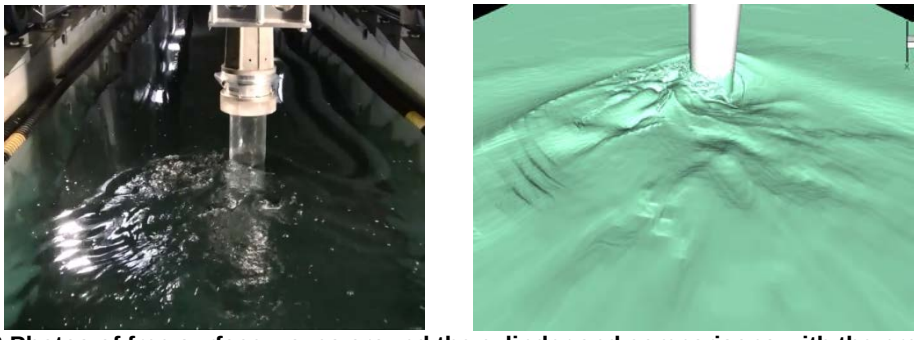

Figure 3-6 Photos of free surface waves around the cylinder and comparisons with the present LES simulations for (Re, Fr, AR, GR) = (123,000, 0.5, 4T, M) at $y=y_{max}$. (fr=1.25)

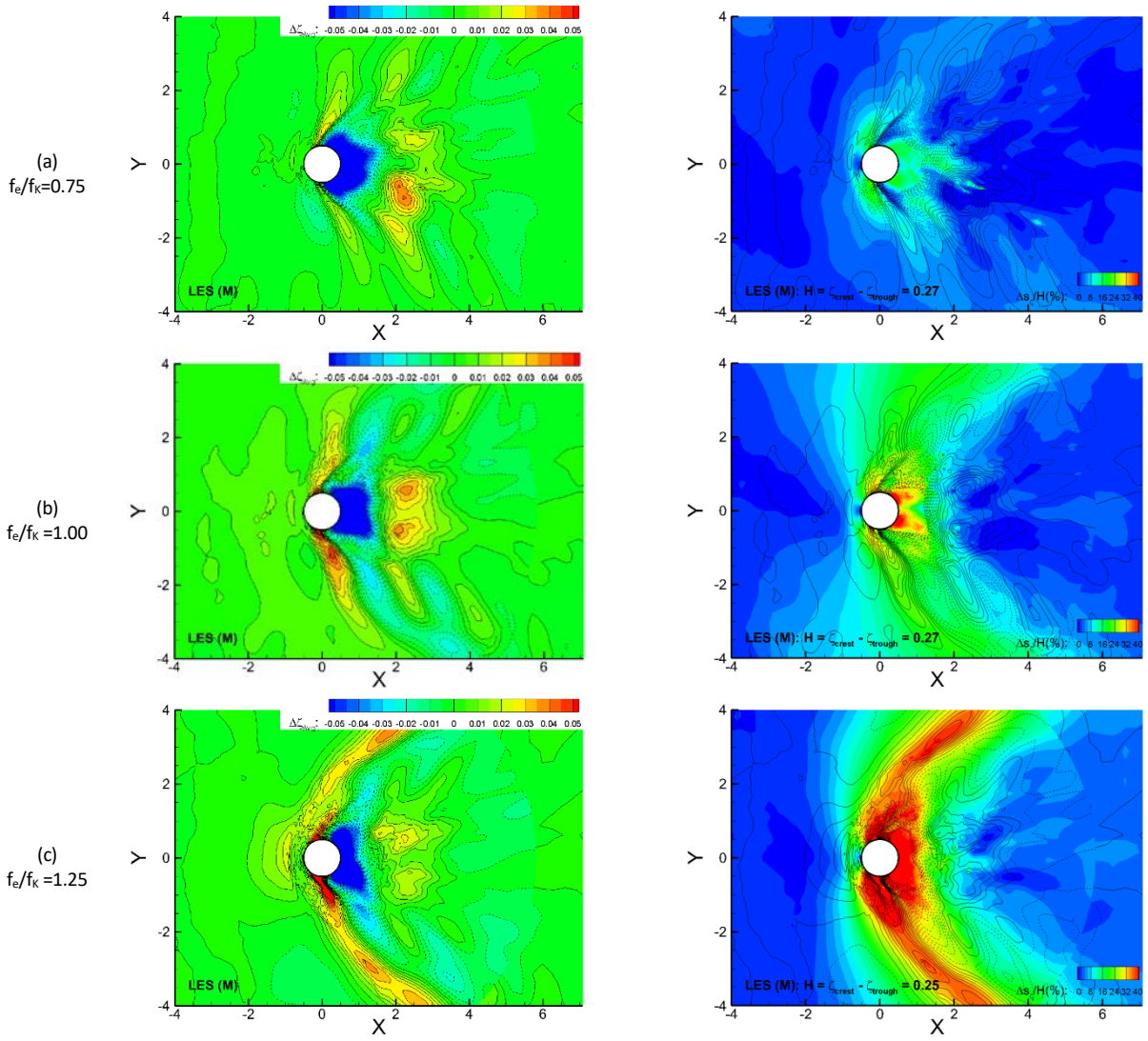

Figure 3-7 Mean and RMS free surface of sway cases subtracted by straight ahead case for (Re, Fr, AR, GR) = (123,000, 0.5, 4T, M): (a) f_e/f_K=0.75, (b) f_e/f_K=1.00, (c) f_e/f_K=1.25.

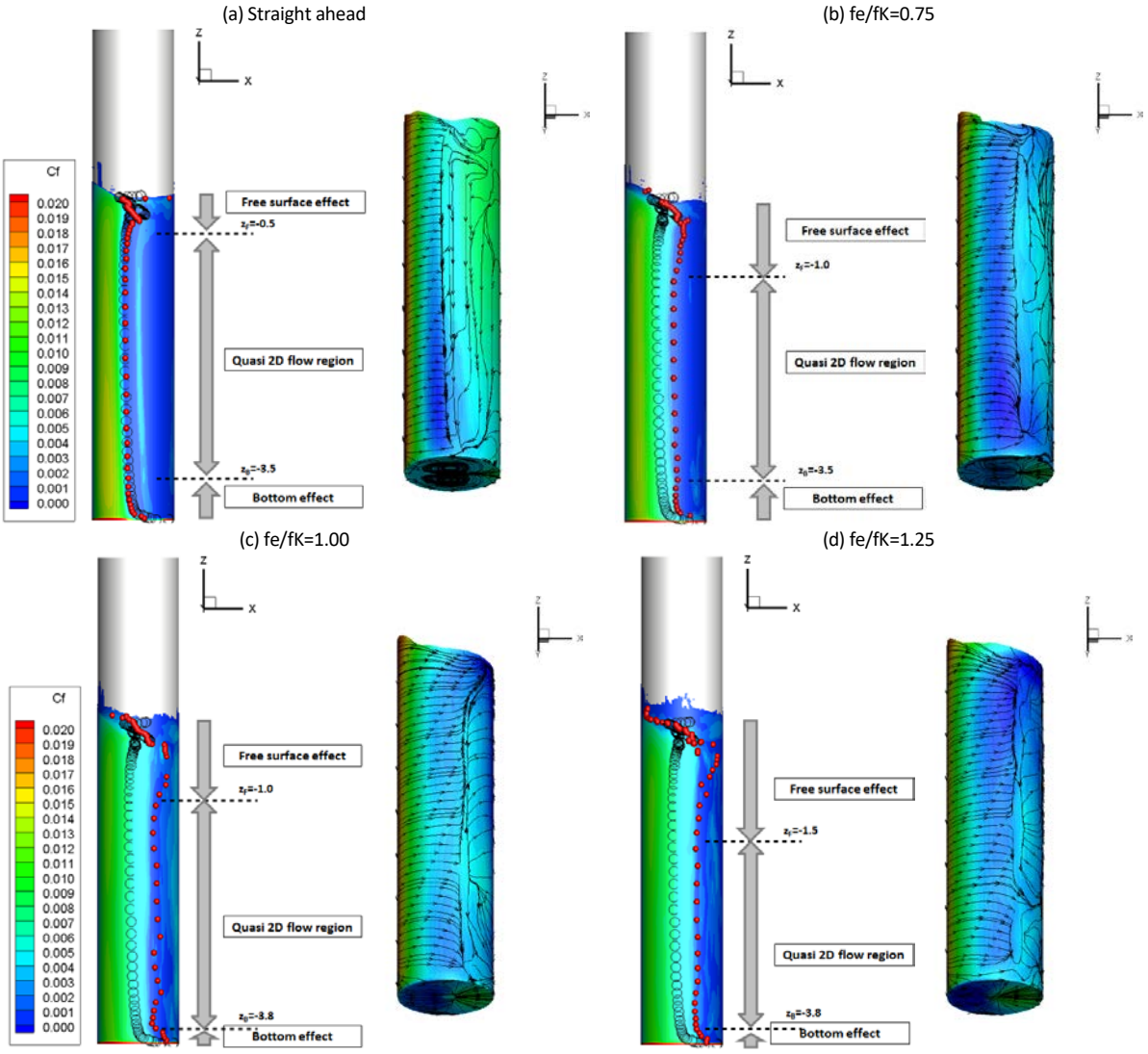

Figure 3-8 Mean Cf contour on cylinder surface with separation angle θ_s (red dot): (a) straight ahead, (b) fe/fK=0.75, (c) fe/fK=1.00, (d) fe/fK=1.25; black circle is separation angle for straight ahead in Stern (2016)

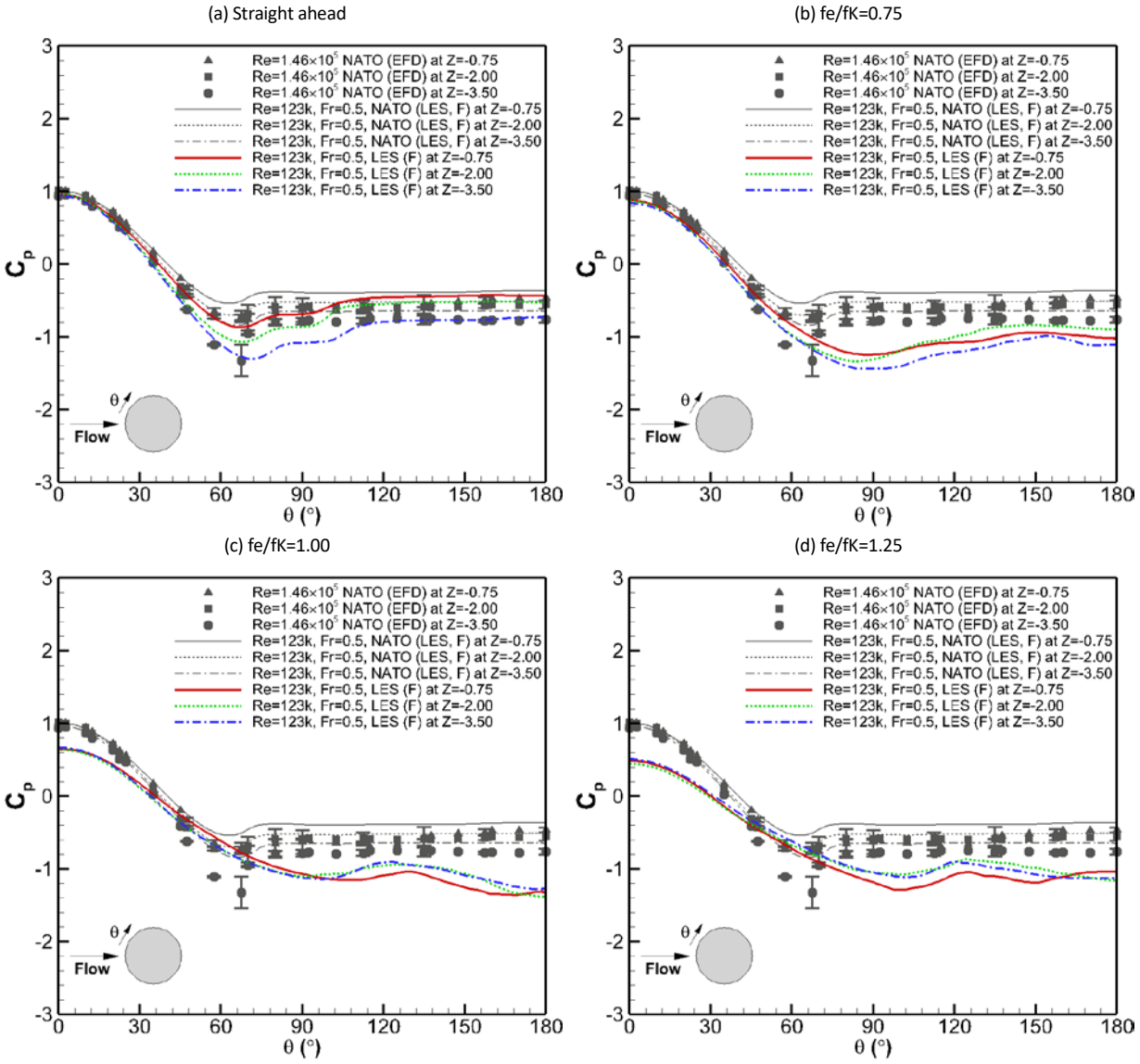

Figure 3-9 Circumferential distributions of Cp according to depth

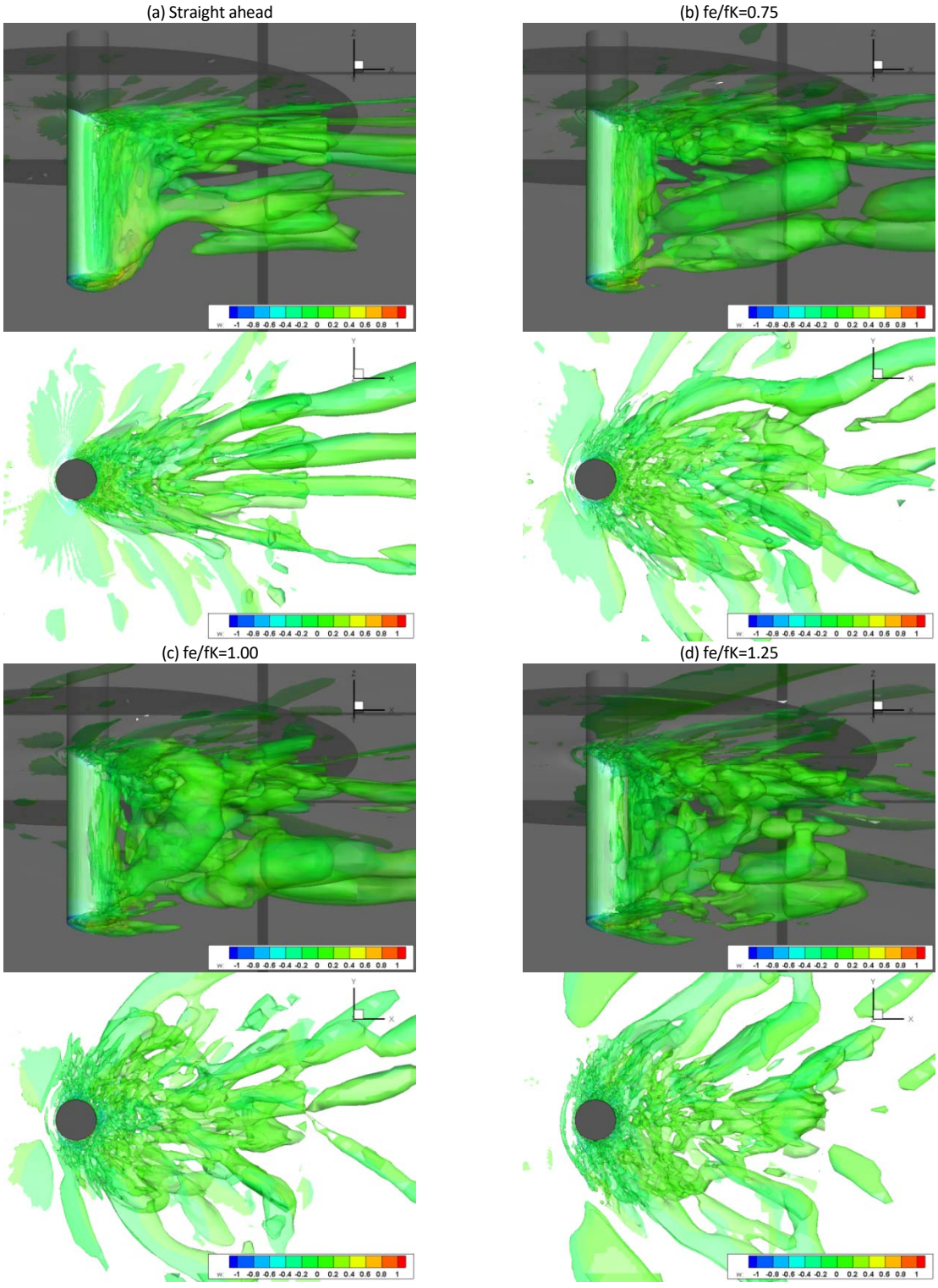

Figure 3-10 Iso-surface of mean Q-criterion (Q=0.04) for (Re, Fr, AR, GR)=(123,000, 0.5, 4T, M): (a) straight ahead, (b) fe/fK=0.75, (c) fe/fK=1.00, (d) fe/fK=1.25

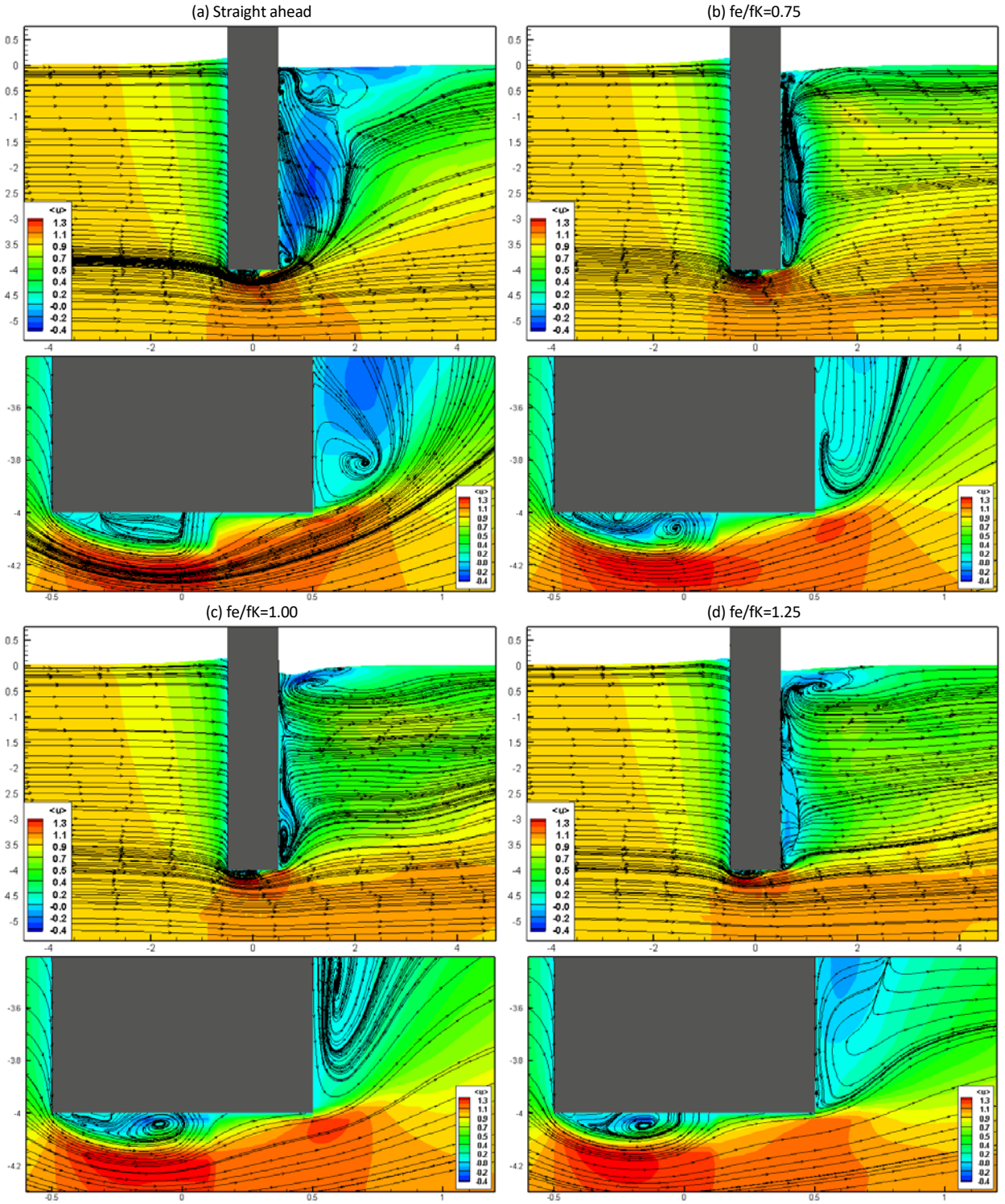

Figure 3-11 Mean streamlines and contours of mean streamwise velocity in the center plane (y=0): lower figures show zoomed-in view near the truncated bottom (Re, Fr, AR, GR)=(123K , 0.5, 4T, M)

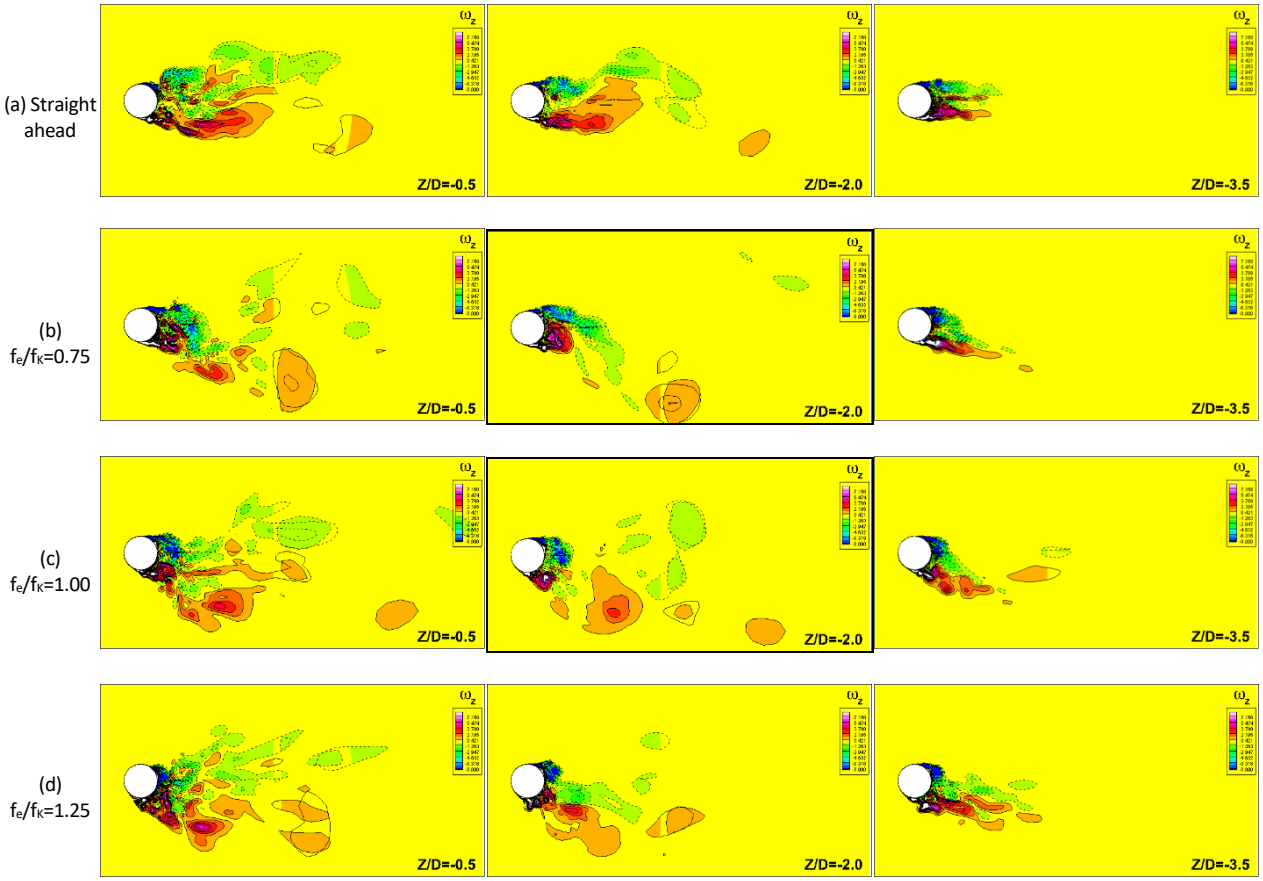

Figure 3-12 Phase-averaged vorticity fields at three vertical locations for (Re, Fr, AR, GR)=(123,000, 0.5, 4T, M) at $y=y_{max}$

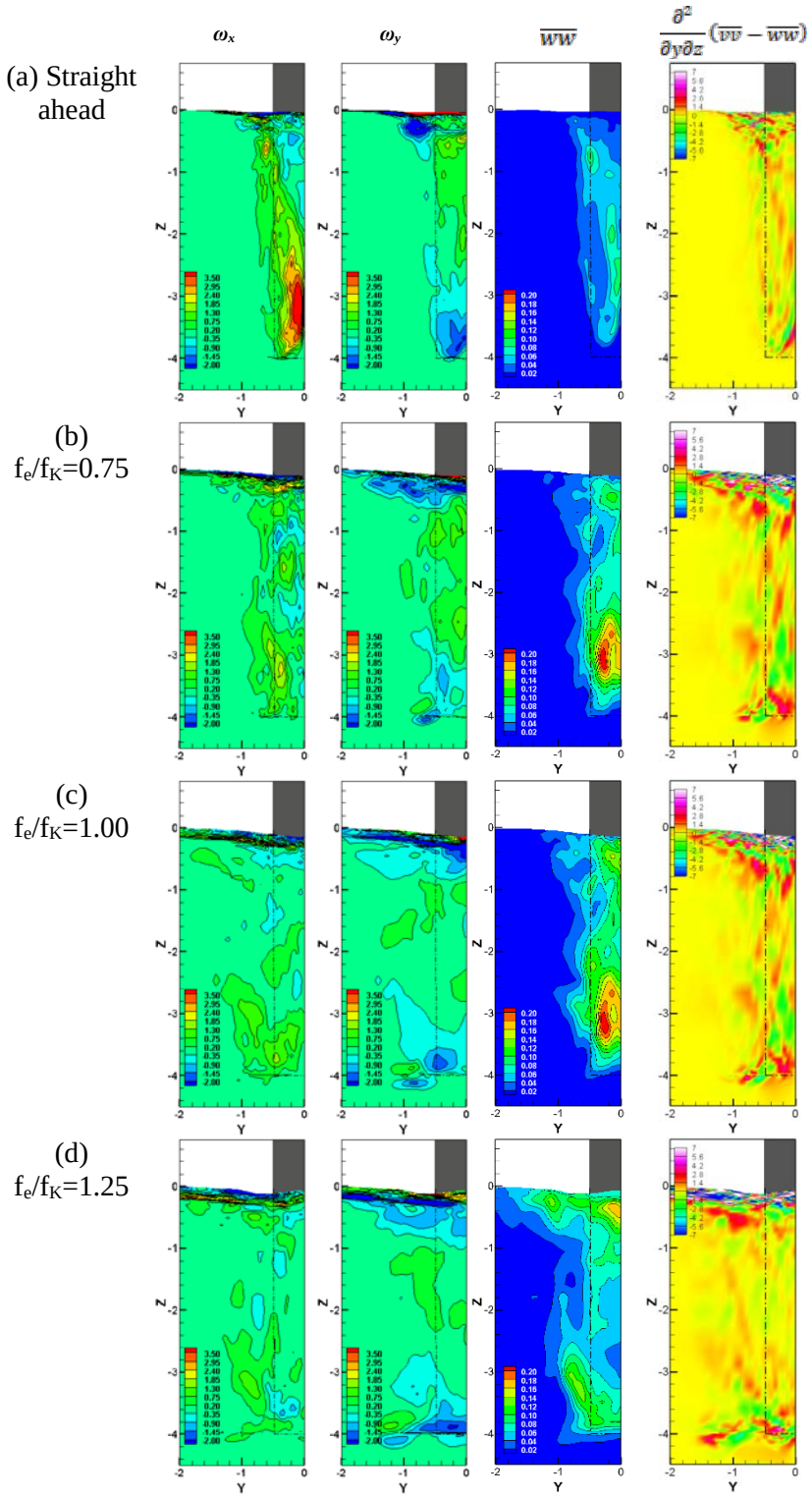

Figure 3-13 Vorticities, Reynolds stresses and gradients of the turbulence anisotropy term at x=1.0 cross-stream plane

APPENDIX A-1 – SDTV CORE TRAJECTORY RECONSTRUCTIONS FOR TPIV 5415 PURE SWAY MEASUREMENTS

Yoon and Stern (2017) presented the core trajectory of SDTV reconstructed from their TPIV measurements for 5415 in a pure sway maneuver. The reconstruction work was based on their earlier work (Yoon et al., 2015b) done for SPIV measurements for 5415 in a pure yaw maneuver. The basic approach by Yoon et al. (2015b) was Fourier Series (FS) expansions of the lateral y- and the vertical z-axis coordinates of the core locations, considering the periodic nature of the hull motions, as well as the physics related with them, which worked reasonably well for the pure yaw condition. However, later NATO AVT-253 has raised questions about the core trajectory data (measured at x = 0.12) to which they were validating their CFD simulation outcomes, and this leads to the present study. A more careful look into the trajectory reconstruction work by Yoon and Stern (2017) has revealed that the goodness-of-fitness of the FS-based reconstructions was not completely satisfactory for the data around the pure sway phase angles 90° or 270° where the transition occurs between the two alternating vortices SDTVP and SDTVS. To overcome this difficulty, the present study presents an alternative approach and discusses the application outcomes.

While the vortices initiate, grow, and dissipate through the pure sway cycles (see Fig. A-1-1 that shows the TPIV axial vorticity ω_x contours through one cycle of the pure sway maneuver, where the red-colored positive ω_x indicates counter-clockwise rotation and the blue-colored negative ω_x clockwise rotation), Figure A-1-2 shows the trail of SDTVS core. The construction of the trail is achieved by overlaying the small portion of the flow that includes the local peak Q (Q_{peak}, i.e., the vortex core) at each phase, through one life cycle of the vortex. From the figure, SDTVS first appears on the starboard side at the location labeled number 9 and with a relatively weaker strength of $Q_{peak} \approx 300$. Then, the vortex traverses to the port side while growing in its strength to reach the maximum $Q_{peak} \approx 18{,}000$ at the location numbered 17. Next, the vortex turns around and traverses back to the starboard side while decreasing in its strength, $Q_{peak} \approx 100$ by the location numbered 27, after which the vortex dissipates.

Figures A-1-3 and A-1-4 show the y- and z-axis coordinates of the core locations through one sway cycle. Herein (and hereafter as well), the red color signifies the counter-clockwise rotating SDTVP and blue color signifies the clockwise rotating SDTVS. It is noted that the TPIV measurements were done only on the starboard side (with a small overlap region across the model center plane, i.e., y = 0). Thus, the points marked with a filled symbol are the real data from the actual measurements, whereas the points with the hollow symbol are the artificial data mirrored from the real data considering the anti-symmetry characteristics of the sway motion. For example, the y values of SDTVP at phases from 78.75° to 112.5° (phase numbers 8 through 11) are the same y values of the SDTVP at phases from 258.75° to 292.5° (phase numbers 24 through 27) with their sign changed. The two different types of (solid vs. dashed) lines are respectively the 4th- or the 6th-order polynomial curve-fits of the data points.

Seemingly, either of the 4th-order or the 6th-order curve-fit can be used. Yet, the outcomes of the core trajectory reconstructions exhibit rather noticeable dissimilarities between the two cases as shown in Figures A-1-5 and A-1-6. The 4th-order case in Figure A-1-5 (and Figure A-1-7) indicates that the vortex makes a ‘sharp turn’ when it turns around its direction at the phase number 17. On the other hand, the 6th-order case shown in Figure A-1-6 (and Figure A-1-8) indicates that the vortex would rather make a ‘go-around’ like loop-shaped turn. Lacking a solid or clear basis on determining which curve-fitting case better reflects the real or true vortex trajectory; the goodness of the curve-fits may be assessed by observing the curve-fit errors between the two cases. For example, when defined that $|E_y| = |y - y^*|/R$ and $|E_z| = |z - z^*|/R$, the average errors were about 2 – 3% for the 4th-order case and about 1 – 2% for the 6th-order case. Here, y* and z* are the curve-fits of y and z and R =

$\sqrt{(y_{max}-y_{min})^2 + (z_{max}-z_{min})^2}$ is the approximate diagonal size of the swept area by the vortex move through the cycle. Table A-1-1 summarizes the results.

Lastly, the following limitations of the present TPIV data should be mentioned: (1) the measurements were only for the starboard side; (2) the bulky size of the TPIV assembly underwater caused a small but non-negligible intrusion to the flow field under measurement; and (3) the imperfect geometrical conditions of the 5415 model for the measurement at that time. Thus, a clear conclusion regarding which case works better between the 4th-order vs the 6th-order fitting cases is deferred and left as on open question. Computational simulations should be a great input toward this question, by visualizing completer and more detailed visualization of the vortex behavior through the sway motion. In addition, the new 4D-PTV measurements should also be a tremendous input, thanks to its greater measurement volume size, very fast data rate, and along with the newly refurbished 5415 model. Figures A-1-9 and A-1-10 provide 2D contour plots of Q at all phase angles and 3D iso-surfaces of Q at all phase angles, which were used in the analysis.

Table A-1-1. Vortex core locations

No.	Phase(°)	Measurement				4th-order polynomial curve-fit						6th-order polynomial curve-fit					
		$STDV_P$		$STDV_S$		$STDV_P$		$STDV_S$				$STDV_P$		$STDV_S$			
		y	z	y	z	y	z	y	z	|Ey|(%R)	|Ez|(%R)	y	z	y	z	Ey(%R)	Ez(%R)
1	0.00	0.0058	-0.0568			0.0054	-0.0570					0.0059	-0.0569				
2	11.25	0.0053	-0.0573			0.0054	-0.0570					0.0057	-0.0571				
3	22.50	0.0053	-0.0573			0.0051	-0.0570					0.0051	-0.0574				
4	33.75	0.0043	-0.0573			0.0045	-0.0572					0.0040	-0.0575				
5	45.00	0.0029	-0.0578			0.0034	-0.0573					0.0027	-0.0576				
6	56.25	0.0014	-0.0573			0.0020	-0.0575					0.0013	-0.0575				
7	67.50	-0.0011	-0.0573			0.0002	-0.0575					-0.0001	-0.0574				
8	78.75					-0.0020	-0.0574					-0.0017	-0.0571				
9	90.00			0.0058	-0.0529	-0.0046	-0.0569	0.0063	-0.0536	2.6%	3.8%	-0.0037	-0.0566	0.0059	-0.0530	0.3%	0.4%
10	101.25			0.0043	-0.0558	-0.0075	-0.0560	0.0040	-0.0553	1.8%	2.6%	-0.0067	-0.0559	0.0041	-0.0559	1.3%	0.4%
11	112.50			0.0019	-0.0578	-0.0108	-0.0544	0.0019	-0.0564	0.3%	7.7%	-0.0117	-0.0546	0.0023	-0.0570	1.9%	4.4%
12	123.75							-0.0001	-0.0570	3.6%	3.7%			0.0004	-0.0572	1.2%	5.0%
13	135.00							-0.0017	-0.0572	1.7%	2.3%			-0.0015	-0.0570	0.4%	1.3%
14	146.25							-0.0031	-0.0572	1.1%	0.3%			-0.0032	-0.0568	0.7%	2.6%
15	157.50							-0.0042	-0.0572	3.4%	2.0%			-0.0046	-0.0567	1.4%	0.4%
16	168.75							-0.0049	-0.0571	2.0%	1.4%			-0.0055	-0.0568	0.9%	0.2%
17	180.00							-0.0054	-0.0570	2.4%	1.0%			-0.0059	-0.0569	0.3%	0.7%
18	191.25							-0.0054	-0.0570	0.8%	1.8%			-0.0057	-0.0571	2.2%	0.8%
19	202.50							-0.0051	-0.0570	0.9%	1.5%			-0.0051	-0.0574	1.4%	0.3%
20	213.75							-0.0045	-0.0572	0.9%	0.7%			-0.0040	-0.0575	1.5%	1.2%
21	225.00							-0.0034	-0.0573	2.8%	2.5%			-0.0027	-0.0576	0.8%	1.2%
22	236.25							-0.0020	-0.0575	3.2%	1.1%			-0.0013	-0.0575	0.3%	1.3%
23	247.50							-0.0002	-0.0575	6.9%	1.4%			0.0001	-0.0574	5.4%	0.4%
24	258.75			0.0009	-0.0578			0.0020	-0.0574	6.3%	2.2%			0.0017	-0.0571	4.4%	3.9%
25	270.00			0.0038	-0.0563	-0.0063	-0.0536	0.0046	-0.0569	4.4%	3.5%	-0.0059	-0.0530	0.0037	-0.0566	0.5%	1.8%
26	281.25			0.0068	-0.0558	-0.0040	-0.0553	0.0075	-0.0560	4.0%	1.1%	-0.0041	-0.0559	0.0067	-0.0559	0.4%	0.6%
27	292.50			0.0117	-0.0548	-0.0019	-0.0564	0.0108	-0.0544	5.1%	2.1%	-0.0023	-0.0570	0.0117	-0.0546	0.1%	0.8%
28	303.75	-0.0006	-0.0563			0.0001	-0.0570					-0.0004	-0.0572				
29	315.00	0.0014	-0.0568			0.0017	-0.0572					0.0015	-0.0570				
30	326.25	0.0033	-0.0573			0.0031	-0.0572					0.0032	-0.0568				
31	337.50	0.0048	-0.0568			0.0042	-0.0572					0.0046	-0.0567				
32	348.75	0.0053	-0.0568			0.0049	-0.0571					0.0055	-0.0568				
									Avg.	2.8%	2.2%				Avg.	1.3%	1.5%

Note: $|Ey|(\%R) = |y - y^*|/R \times 100$; $|Ez|(\%R) = |z - z^*|/R \times 100$, where y* and z* are the polynomial fit of y and z, respectively, and $R = \mathrm{sqrt}((y_{max} - y_{min})^2 + (z_{max} - z_{min})^2)$.

Figure A-1-1. Axial vorticity (ω_x) contours.

γ = 0° (S1+ P17; β = 10°)	γ = 11.25° (S2+ P18)	γ=22.5° (S3+ P19)	γ = 33.75° (S4+ P20)
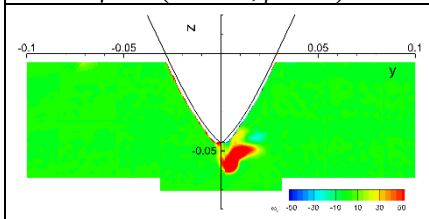	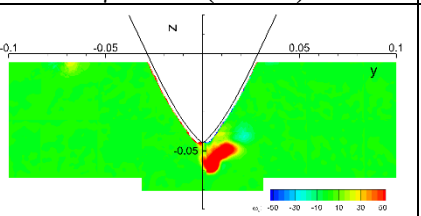	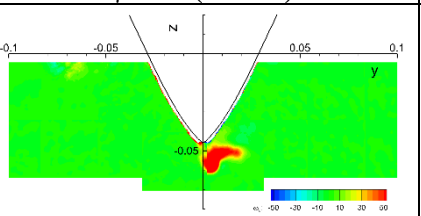	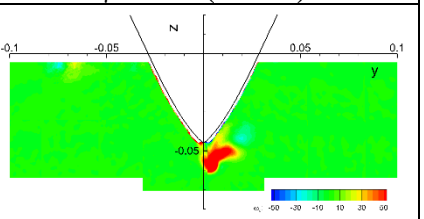
γ = 45° (S5+ P21)	γ = 56.25° (S6+ P22)	γ = 67.5° (S7+ P23)	γ = 78.75° (S8+ P24)
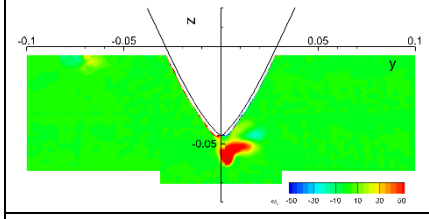	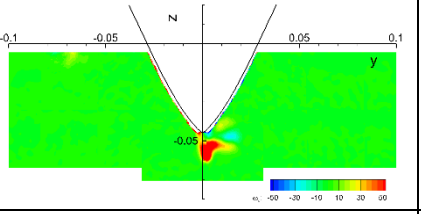	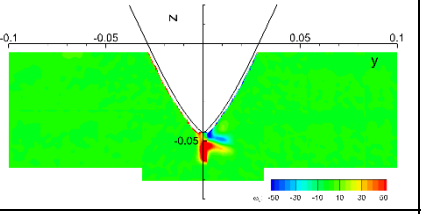	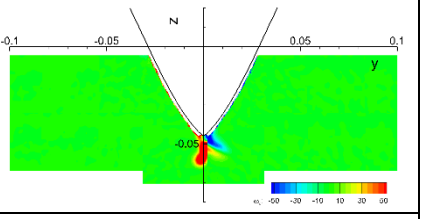
γ = 90° (S9+ P25; β = 0°)	γ = 101.25° (S10+ P26)	γ = 112.5° (S11+ P27)	γ = 123.75° (S12+ P28)
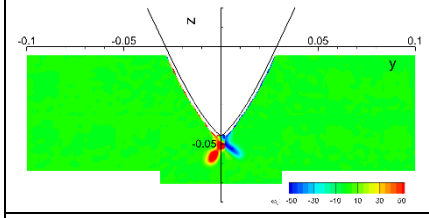	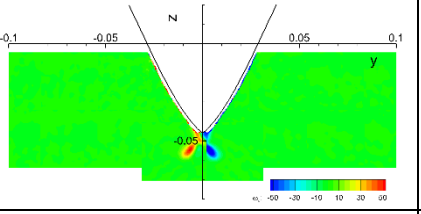	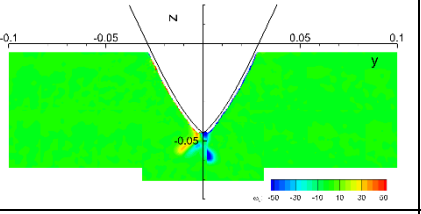	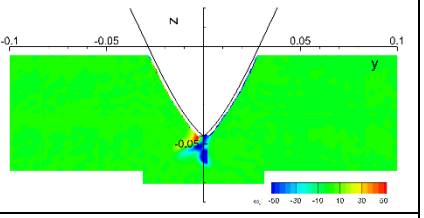
γ = 135° (S13+ P29)	γ = 146.25° (S14+P30)	γ = 157.5° (S15+ P31)	γ = 168.75° (S16+ P32)
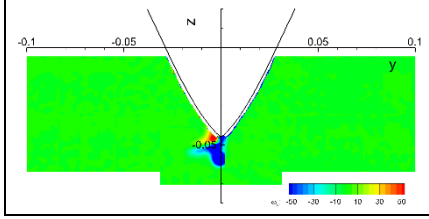	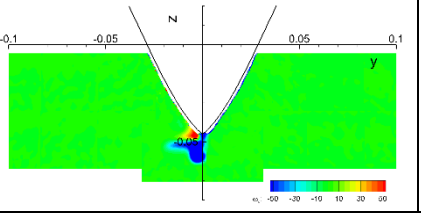	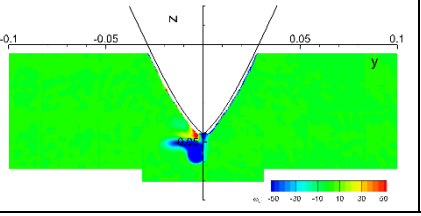	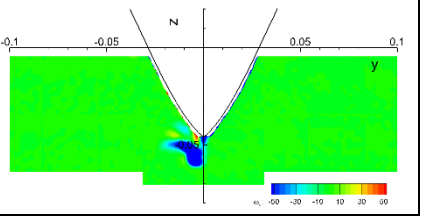

**Snn = Starboard measurement at the nn-th phase (out 32); Pmm = Portside at the nn-th phase mirrored from the mm-th phase starboard measurement.*

Figure A-1-1. Continued.

γ = 180° (S17+P1; β = -10°)	γ = 191.25° (S18+P2)	γ = 202.5° (S19+P3)	γ = 213.75° (S20+P4)
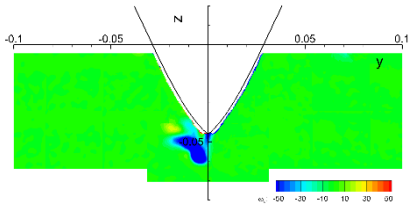	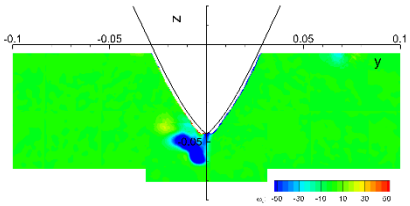	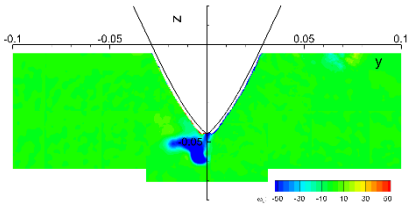	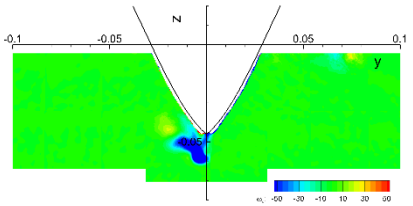
γ = 225° (S21+P5)	γ = 236.25° (S22+P6)	γ = 247.5° (S23+P7)	γ = 258.75° (S24+P8)
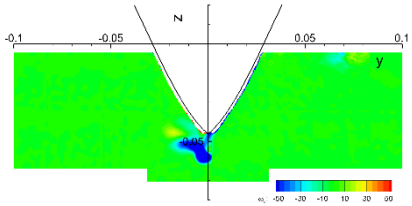	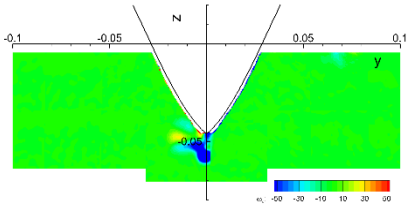	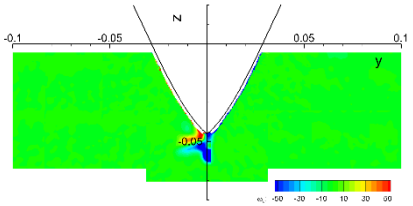	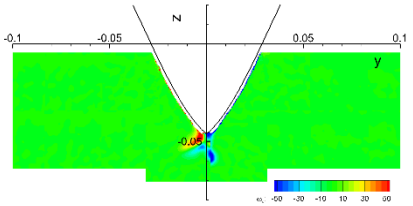
γ = 270° (S25+P9; β = 0°)	γ = 281.25° (S26+P10)	γ = 292.5° (S27+P11)	γ = 303.75° (S28+P12)
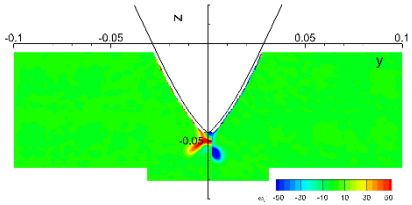	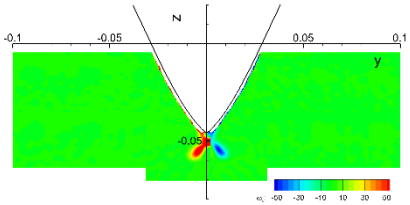	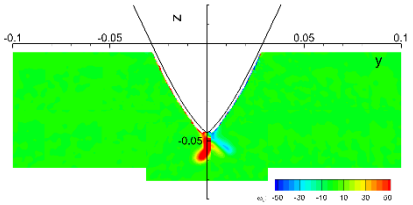	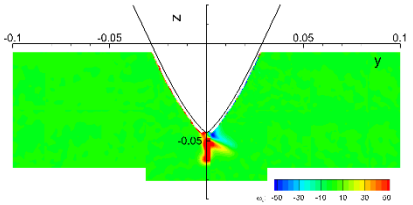
γ = 315° (S29+P13)	γ = 326.25° (S30+P14)	γ = 337.5° (S31+P15)	γ = 348.75° (S32+P16)
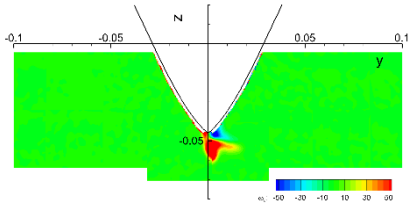	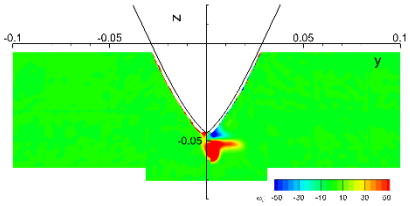	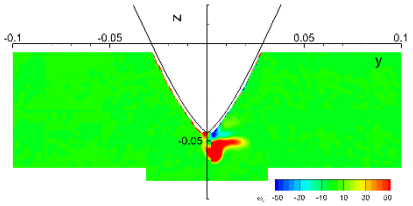	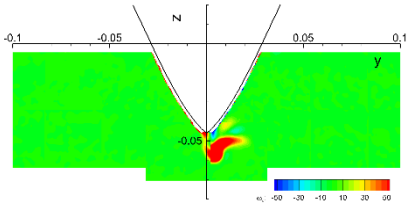

**Snn = Starboard measurement at the nn-th phase (out 32); Pmm = Portside at the nn-th phase mirrored from the mm-th phase starboard measurement.*

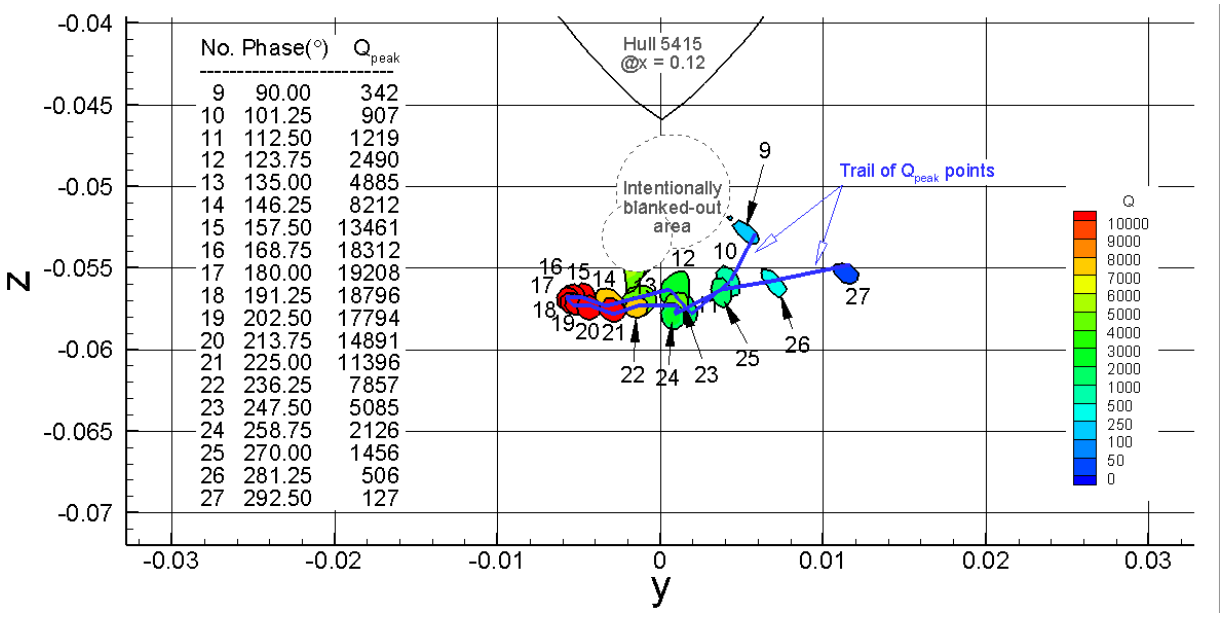

Figure A-1- 2. Trail of local Q peak points (i.e. the vortex core locations) of SDTVS.

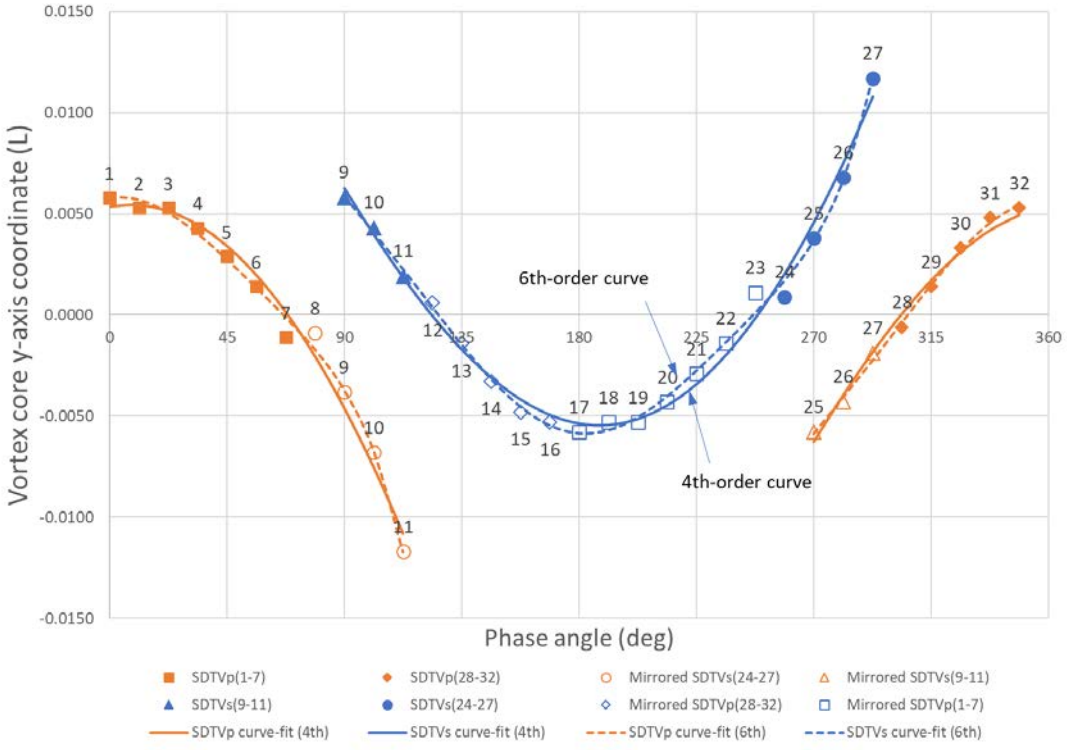

Figure A-1-3. The y-coordinates of STDV core locations through one pure sway cycle and their curve-fits.

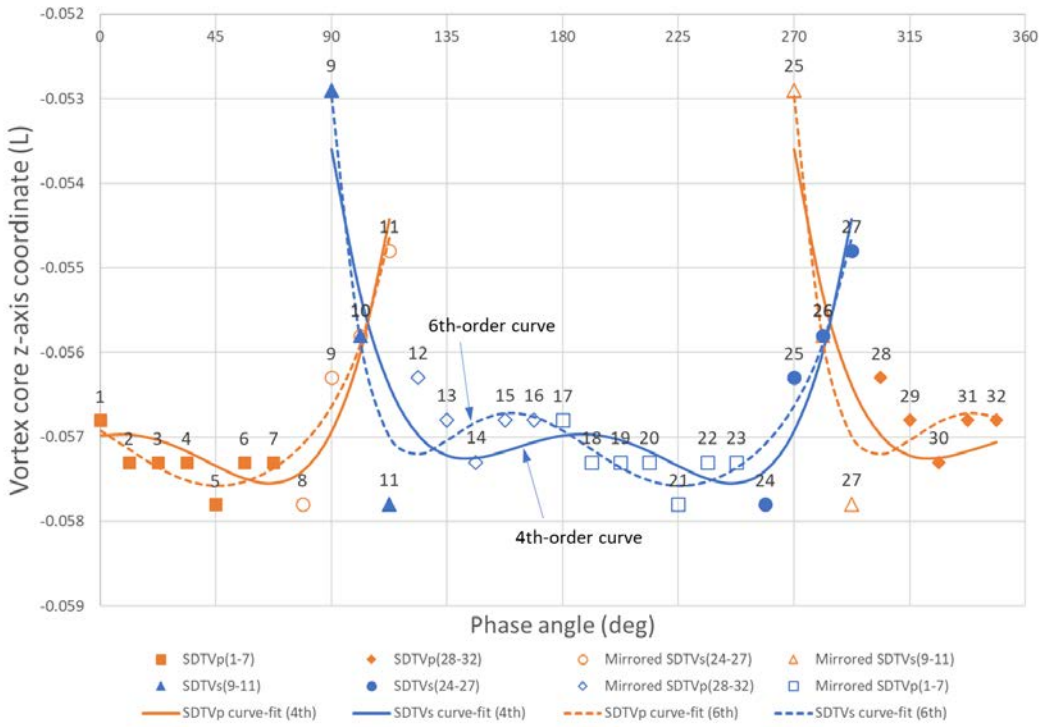

Figure A-1-4. The z-coordinates of STDV core locations through one pure sway cycle and their curve-fits.

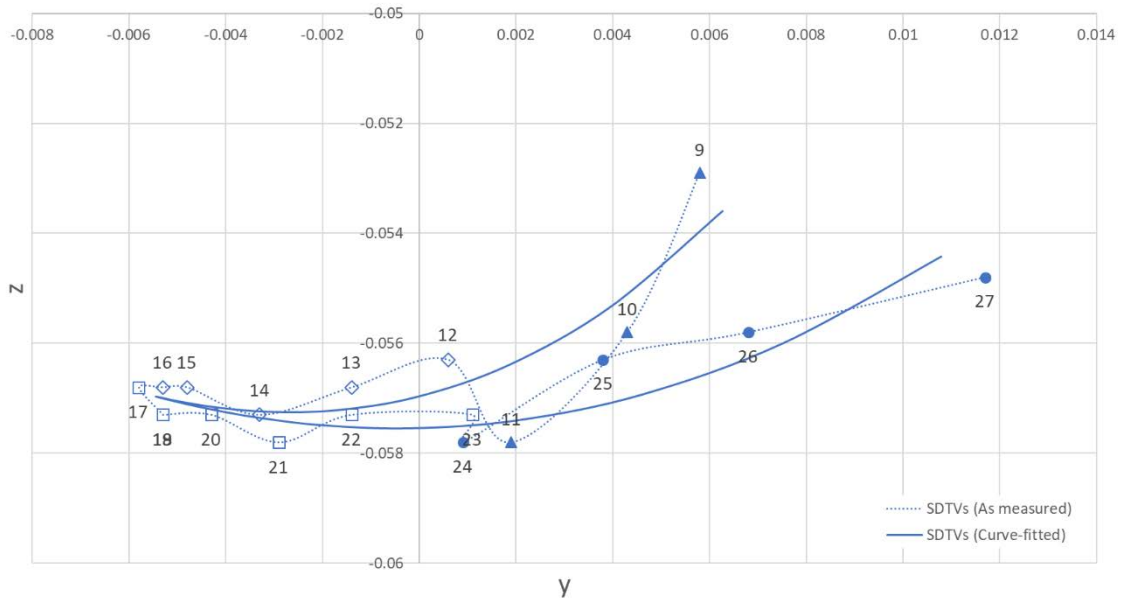

Figure A-1-5. SDTVS core trajectories using the measured data vs. reconstruction using the 4th-order polynomial curve-fit.

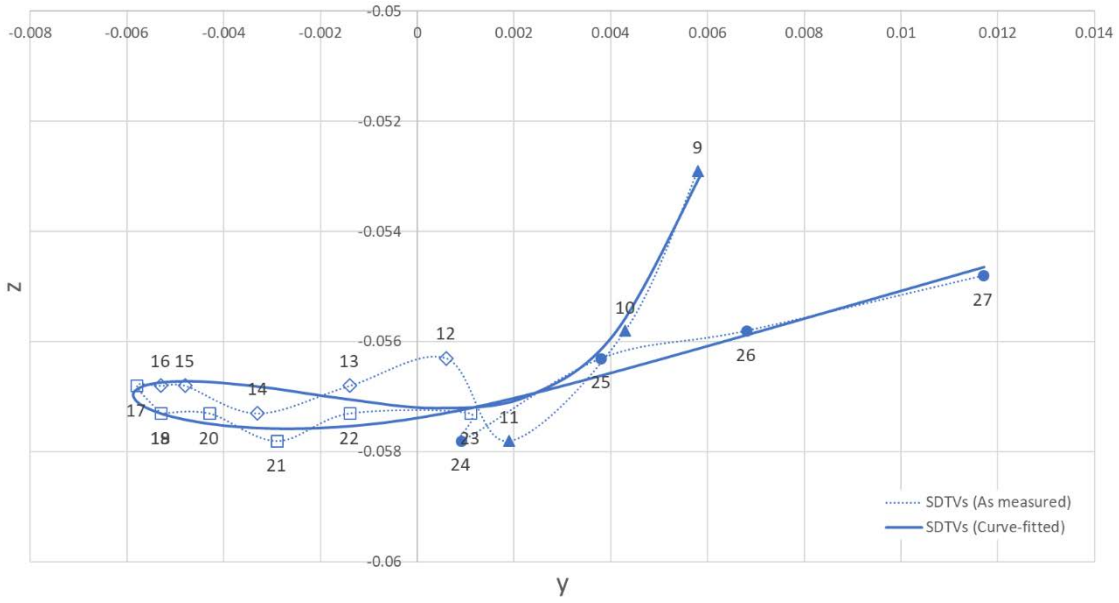

Figure A-1-5. SDTVS core trajectories using the measured data vs. reconstruction using the 6th-order polynomial curve-fit.

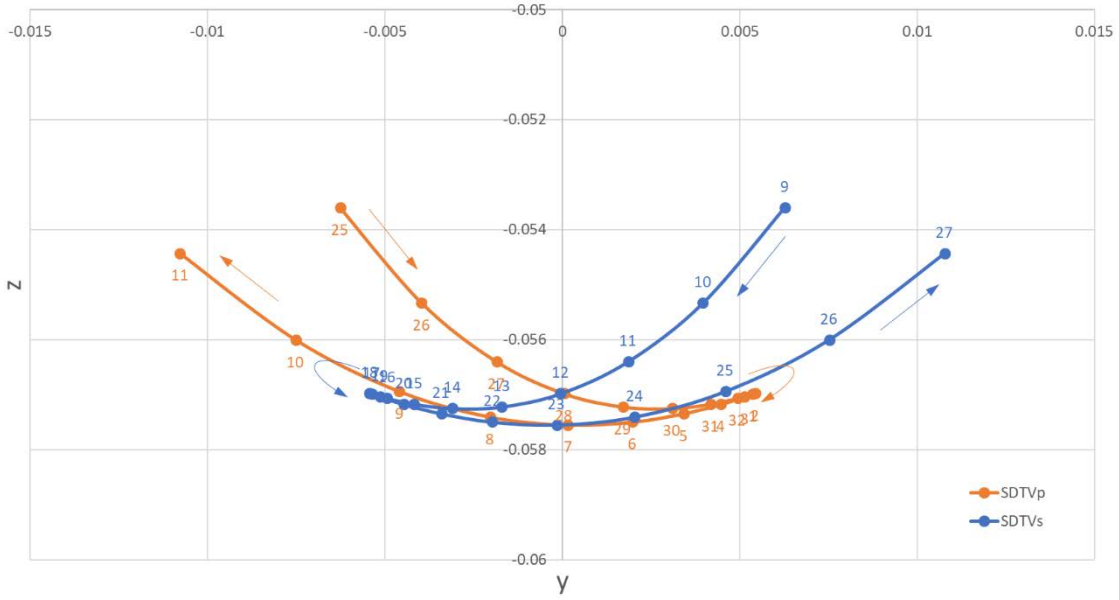

Figure A-1-7. Reconstructed core trajectories of SDTVP (blue) & SDTVPS (red) using the 4th-order polynomial curve-fits.

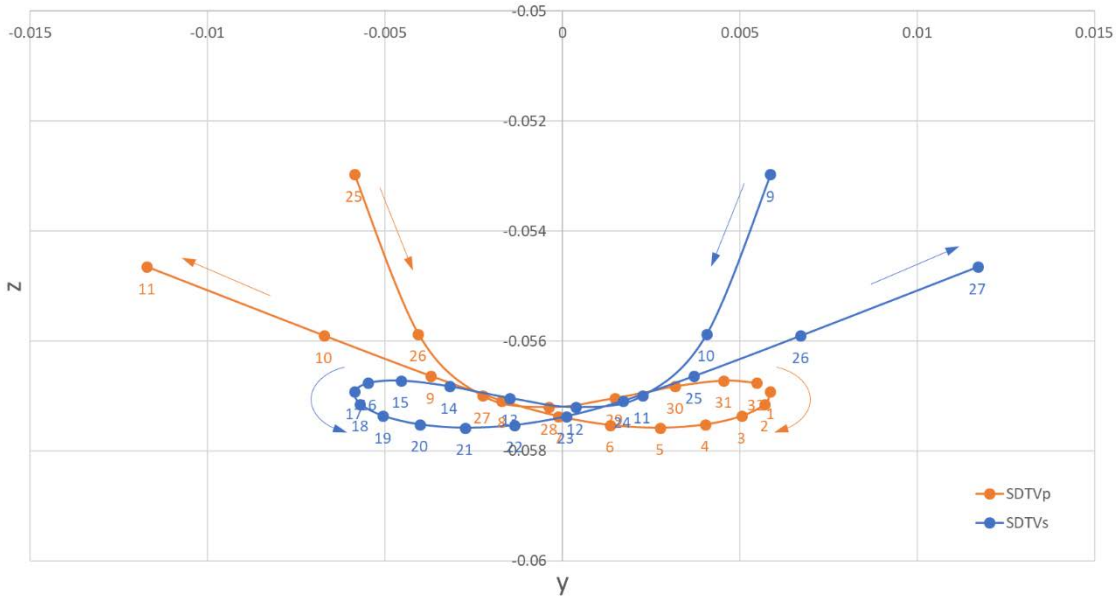

FigureA-1-8. Reconstructed core trajectories of SDTVP (blue) & SDTVPS (red) using the 6th-order polynomial curve-fits.

Figure A-1-9. 2D contour plots of Q at all phase angles

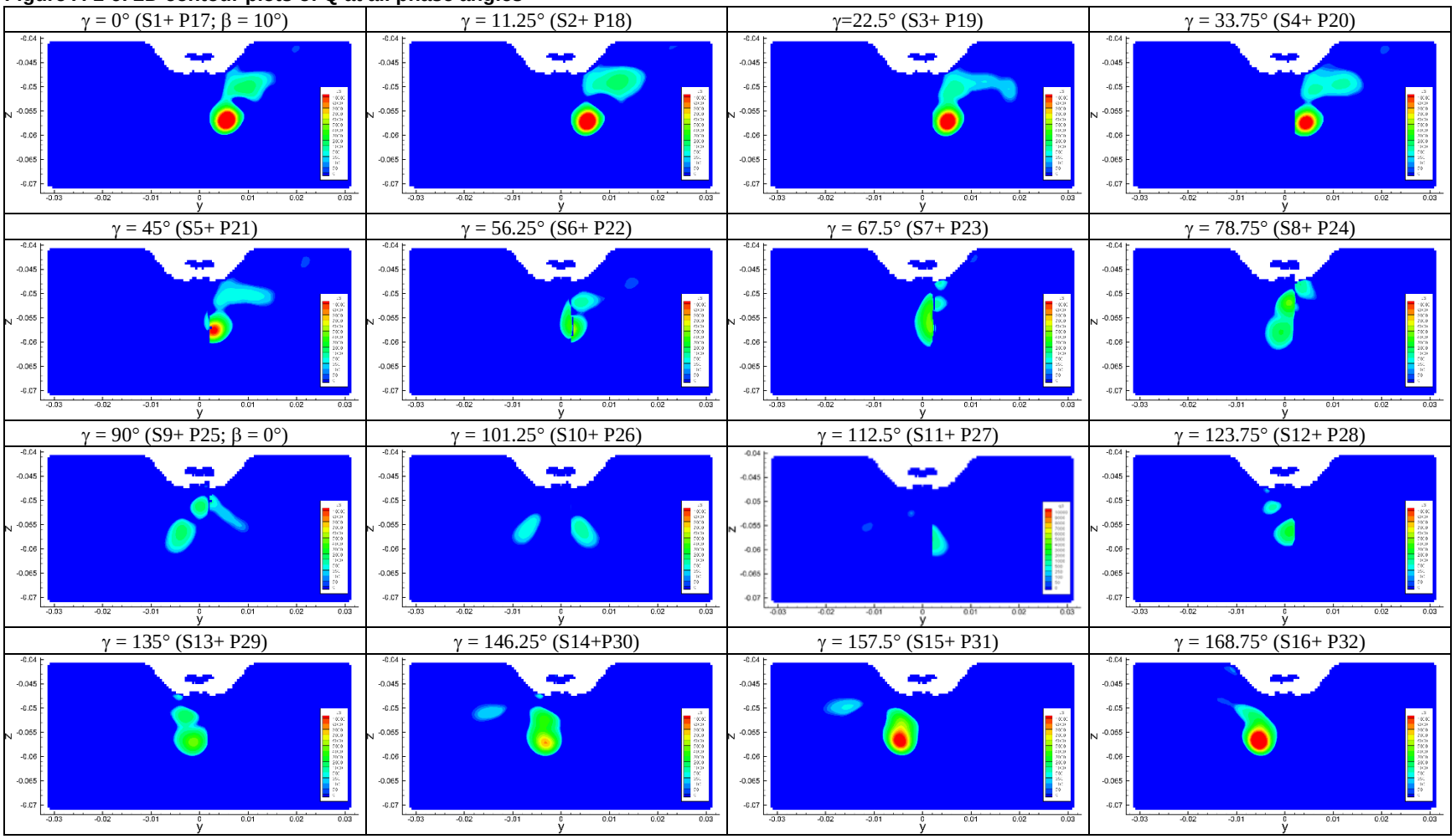

Figure A-1-9 Contd. - 2D contour plots of Q at all phase angles

γ = 180° (S17+P1; β = -10°)	γ = 191.25° (S18+P2)	γ = 202.5° (S19+P3)	γ = 213.75° (S20+P4)
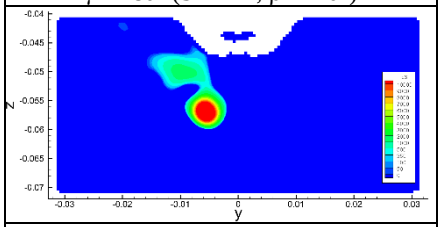	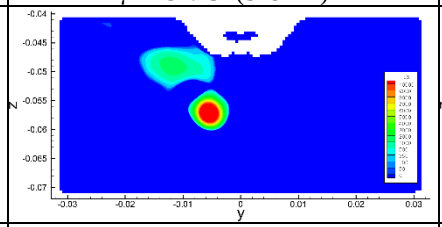	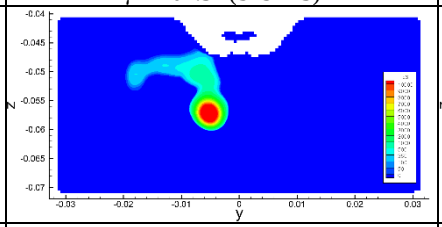	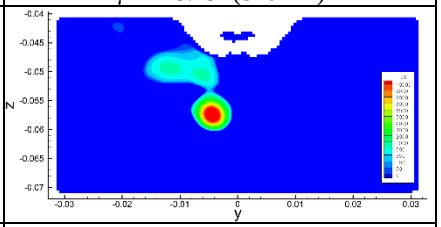
γ = 225° (S21+P5)	γ = 236.25° (S22+P6)	γ = 247.5° (S23+P7)	γ = 258.75° (S24+P8)
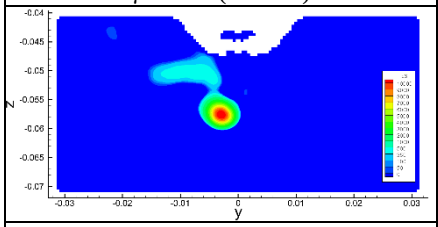	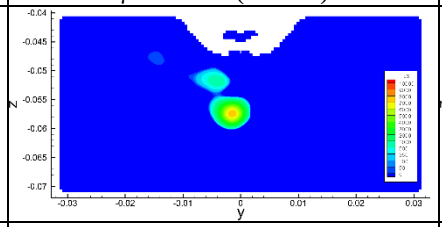	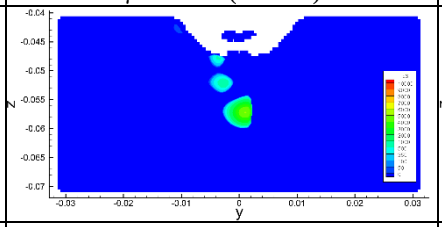	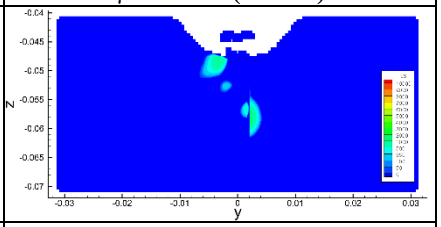
γ = 270° (S25+P9; β = 0°)	γ = 281.25° (S26+P10)	γ = 292.5° (S27+P11)	γ = 303.75° (S28+P12)
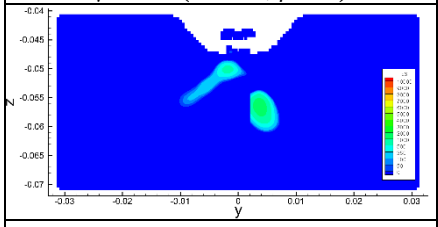	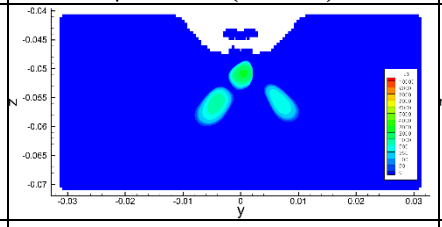	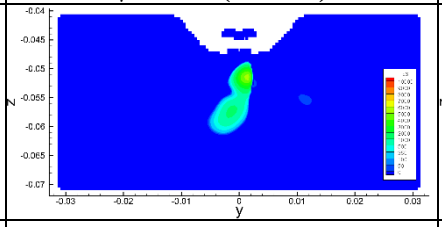	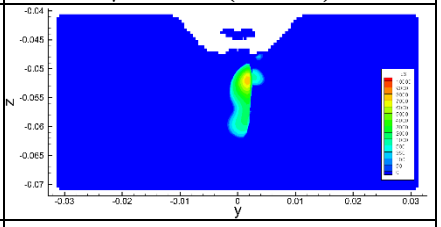
γ = 315° (S29+P13)	γ = 326.25° (S30+P14)	γ = 337.5° (S31+P15)	γ = 348.75° (S32+P16)
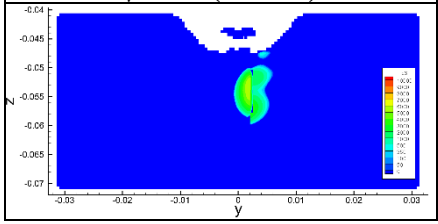	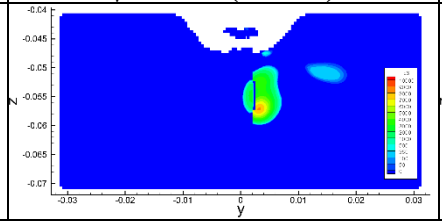	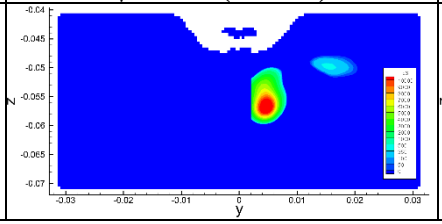	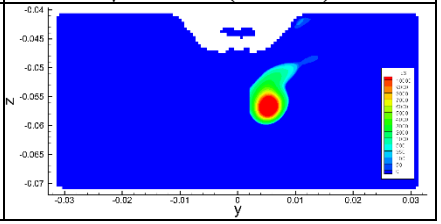

Figure A-1-10. 3D iso-surfaces of Q at all phase angles

γ = 0° (S1+ P17; β = 10°)	γ = 11.25° (S2+ P18)	γ=22.5° (S3+ P19)	γ = 33.75° (S4+ P20)
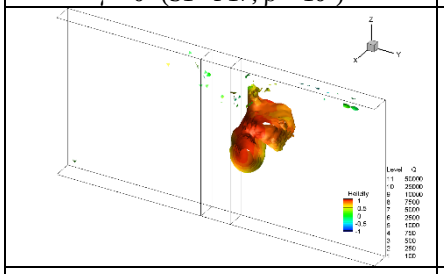	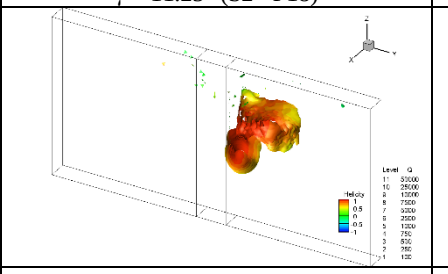	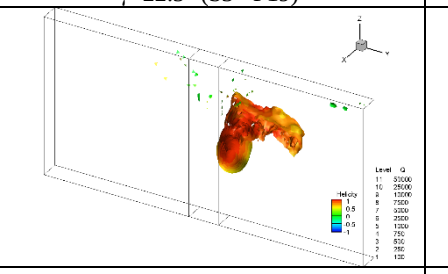	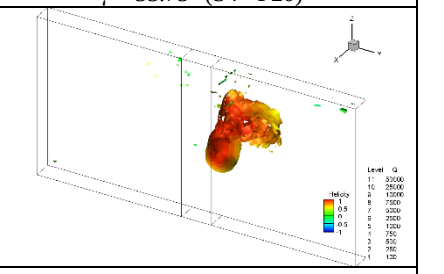
γ = 45° (S5+ P21)	γ = 56.25° (S6+ P22)	γ = 67.5° (S7+ P23)	γ = 78.75° (S8+ P24)
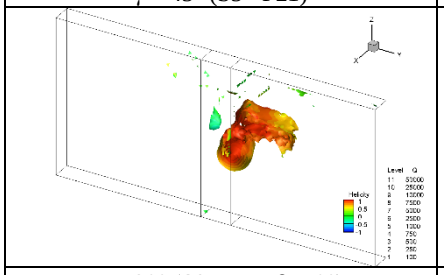	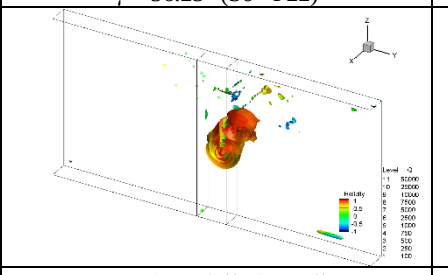	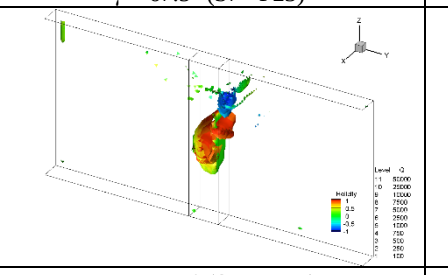	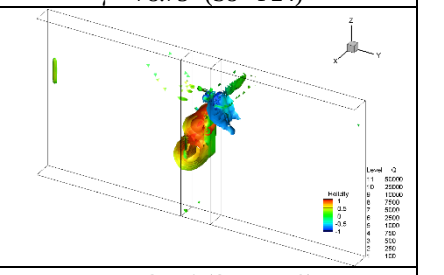
γ = 90° (S9+ P25; β = 0°)	γ = 101.25° (S10+ P26)	γ = 112.5° (S11+ P27)	γ = 123.75° (S12+ P28)
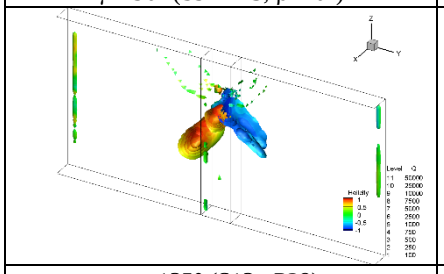	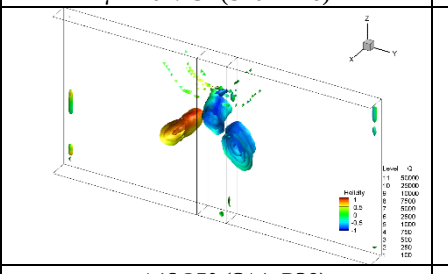	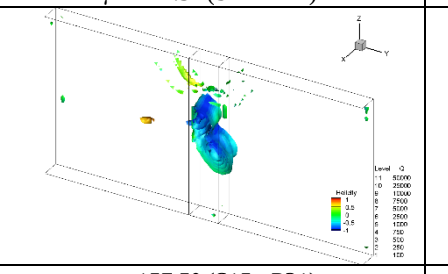	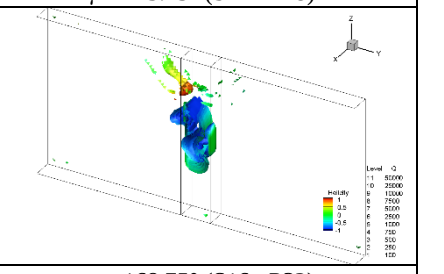
γ = 135° (S13+ P29)	γ = 146.25° (S14+P30)	γ = 157.5° (S15+ P31)	γ = 168.75° (S16+ P32)
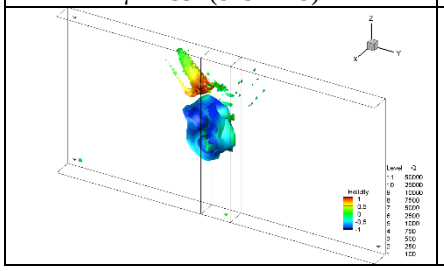	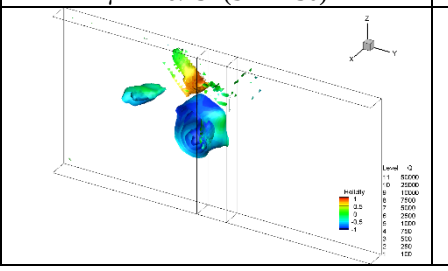	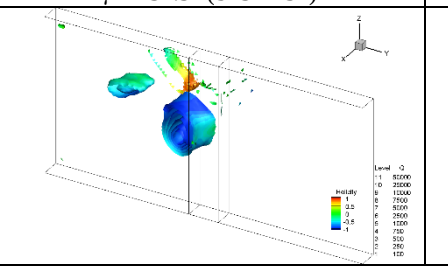	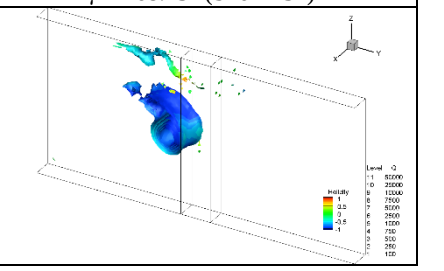

Figure A-1-10. Contd. - 3D iso-surfaces of Q at all phase angles

γ = 180° (S17+P1; β = -10°)	γ = 191.25° (S18+P2)	γ = 202.5° (S19+P3)	γ = 213.75° (S20+P4)
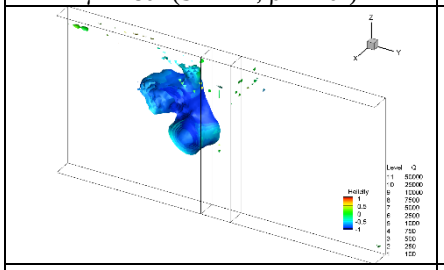	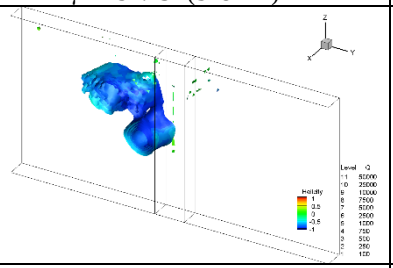	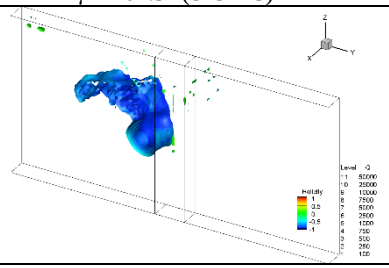	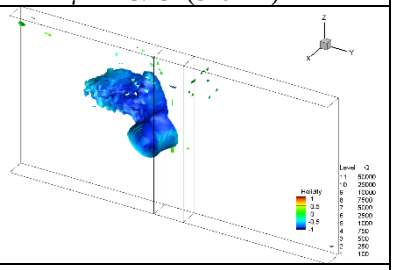
γ = 225° (S21+P5)	γ = 236.25° (S22+P6)	γ = 247.5° (S23+P7)	γ = 258.75° (S24+P8)
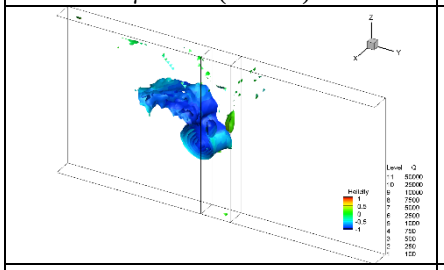	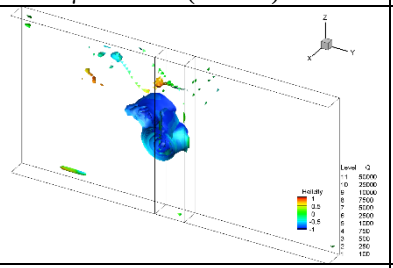	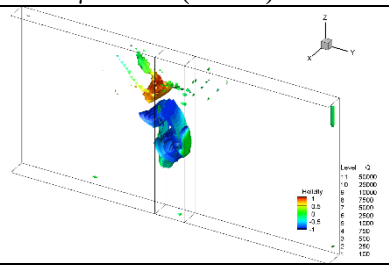	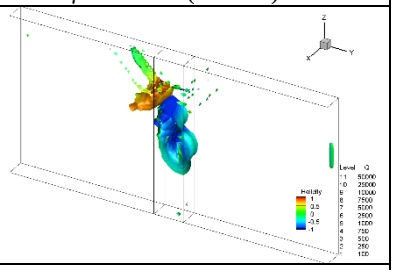
γ = 270° (S25+P9; β = 0°)	γ = 281.25° (S26+P10)	γ = 292.5° (S27+P11)	γ = 303.75° (S28+P12)
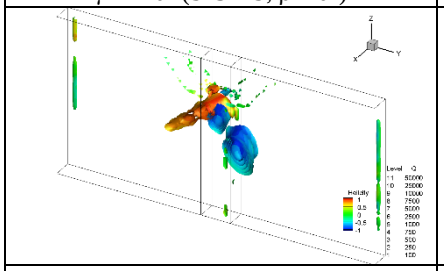	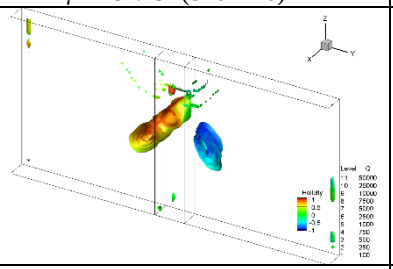	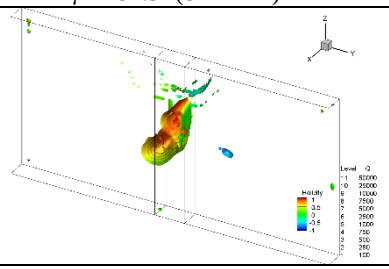	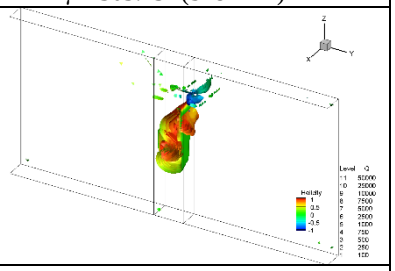
γ = 315° (S29+P13)	γ = 326.25° (S30+P14)	γ = 337.5° (S31+P15)	γ = 348.75° (S32+P16)